

1 **2021 North American Heatwave Amplified by Climate-Change-Driven Nonlinear**  
2 **Interactions**

3

4 Samuel Bartusek<sup>\*1,2</sup>, Kai Kornhuber<sup>2,3</sup>, Mingfang Ting<sup>2</sup>

5 1. Department of Earth and Environmental Sciences, Columbia University, New York, NY,  
6 USA

7 2. Lamont-Doherty Earth Observatory, Columbia University, Palisades, NY, USA

8 3. German Council on Foreign Relations, DGAP, Berlin, Germany

9

10 \*Corresponding author: Samuel Bartusek, [samuel.bartusek@columbia.edu](mailto:samuel.bartusek@columbia.edu)

11

12

13 **Abstract**

14 Heat conditions in North America in summer 2021 exceeded prior heatwaves by margins many  
15 would have considered impossible under current climate conditions. Associated severe impacts  
16 highlight the need for understanding the heatwave's physical drivers and relations to climate  
17 change, to improve the projection and prediction of future extreme heat risks. Here, we find that  
18 slow- and fast-moving components of the atmospheric circulation interacted, along with regional  
19 soil moisture deficiency, to trigger a 5-sigma heat event. Its severity was amplified ~40% by  
20 nonlinear interactions between its drivers, likely driven by land-atmosphere feedbacks catalyzed  
21 by long-term regional warming and soil drying. Since the 1950s, global warming has  
22 transformed the event's peak daily regional temperature anomaly from virtually impossible to a  
23 presently-estimated ~200-yearly occurrence. Its likelihood is projected to increase rapidly with  
24 further global warming, possibly becoming a 10-yearly occurrence in a climate 2°C warmer than  
25 preindustrial, which may be reached by 2050.

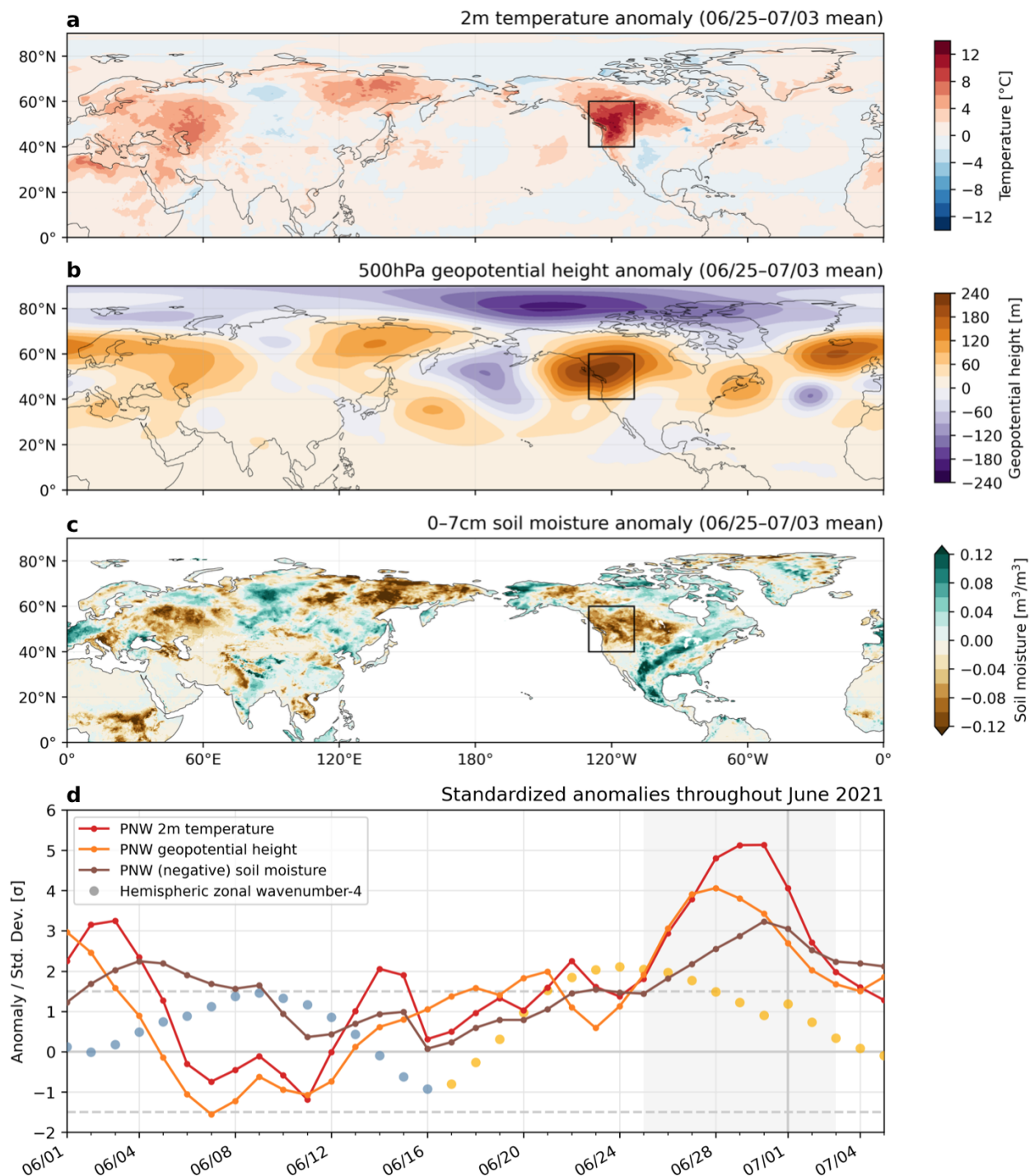
26 **Main**

27 Unprecedented heat conditions in the North American Pacific Northwest (PNW) in late June and  
28 early July 2021 affected millions, likely led to deaths in the thousands, and promoted wildfires  
29 affecting air quality throughout the continent. CDC records suggest hundreds of excess deaths in  
30 both Washington and Oregon during the heatwave, with hundreds more in British Columbia  
31 officially attributed to heat, likely undercounting the true toll<sup>1,2,3</sup>. Heat-related emergency room  
32 visits spiked, totaling nearly 3,000 over June 25–30 in the US PNW<sup>4</sup>. The affected region’s high  
33 vulnerability to extreme heat amplified its dangers: air conditioning access in the Seattle and  
34 Portland metropolitan areas is among the lowest in the country<sup>5</sup>, while many PNW counties have  
35 among the largest outdoor agricultural worker populations and highest social vulnerability in the  
36 country<sup>6</sup>. Exacerbated by drought conditions (covering 95% of the US PNW by June 22<sup>7</sup>),  
37 wildfires sparked during and following the heatwave constituted some of 93 large fires  
38 contributing to millions of western US acres burned by August<sup>8</sup>. Wildfire smoke caused  
39 particulate matter pollution across the continent, for instance contributing to New York City’s  
40 worst air quality in 15 years<sup>9</sup>.

41 Even as global warming increases the severity and frequency of heatwaves<sup>10,11</sup>, the  
42 magnitude of this event exceeded what many may have considered plausible under current  
43 climate conditions<sup>12</sup>. While heat records are typically broken by small increments<sup>13,14</sup>, this event  
44 shattered records by tens of degrees Celsius<sup>15</sup>. Such an unprecedented event<sup>16</sup> raises the pressing  
45 question of whether heat extremes’ future projections are too conservative or their mechanisms  
46 inadequately captured by climate models. It is therefore important to understand the event’s  
47 physical drivers and assess their connections with climate change. From an attribution  
48 perspective, was this anomaly so extreme to be considered virtually impossible regardless of  
49 climate change (a “black swan” event<sup>17,18</sup>), or was it plausible and foreseeable, and even made  
50 more likely due to baseline warming (a “gray swan”<sup>19</sup>)? Further, were its drivers mechanistically  
51 altered by climate trends, beyond their occurrence in a warming background—perhaps indicating  
52 exacerbated future risk?

53 Whether any change in atmospheric dynamics or land–atmosphere interaction is  
54 implicated in amplifying current and future heat extremes is a persistent question: common  
55 heatwave mechanisms may be modified by climate change beyond a shift in background  
56 conditions. Mid-latitude heat extremes, typically triggered by anticyclonic circulation anomalies,

57 have often been associated with persistently-amplified planetary-scale atmospheric waves<sup>20–24</sup>.  
58 Conditions favorable for wave amplification may become more frequent, possibly connected to  
59 weakening of the north-south temperature gradient<sup>25–27</sup>. Additionally, thermodynamic land–  
60 atmosphere feedbacks can strongly amplify heatwave temperatures, often involving nonlinear  
61 processes<sup>28–32</sup>. Land areas typically occupy two distinct regimes of soil–atmosphere interaction:  
62 areas where soil moisture is too high or too low for its variability to affect evapotranspiration,  
63 versus areas with “transitional” climates (between wet and dry), where soil moisture variability  
64 affects evapotranspiration and therefore temperature<sup>33</sup>. The central US is a noted transitional-  
65 climate hotspot of strong soil moisture–temperature coupling<sup>33,34</sup>, but although the presently-wet  
66 PNW is projected to dry due to warming<sup>35–37</sup>, and aridification of other wet regions has been  
67 implicated in amplifying summer temperature variability (e.g. central Europe<sup>38</sup>), the PNW has  
68 not garnered similar focus on land–atmosphere contributions to its temperature variability and  
69 their potential changes.



70 **Fig. 1: Timing and location of the PNW heatwave and its associated atmospheric dynamical**  
 71 **and land-surface conditions.** Northern Hemisphere **a)** Temperature, **b)** geopotential height, and  
 72 **c)** soil moisture anomalies during the 2021 PNW heatwave (June 25–July 3), and **d)** their  
 73 evolution throughout June averaged over the PNW (black box in **a-c**); 40–60°N, 110–130°W;  
 74 land temperature only). During the heatwave, much of the PNW experienced extreme anomalies  
 75 in temperature, geopotential height, and soil moisture exceeding 5, 4, and 3 standard deviations

76 *from their 1981–2010 means. d) also shows the amplitude of a zonal-wavenumber-4 disturbance*  
77 *in the midlatitude upper-atmospheric circulation, colored blue when in negative phase and*  
78 *yellow in positive phase (see Methods). This wave corresponds to 4 regions of positive*  
79 *(alternating with 4 negative) geopotential height anomalies encircling the hemisphere, visible in*  
80 *a–c) with associated temperature and soil moisture anomalies affecting the PNW, central*  
81 *Eurasia, and Northeastern Siberia. See Extended Data Fig. 1 for a detailed perspective on the*  
82 *evolution of atmosphere dynamical aspects.*

83

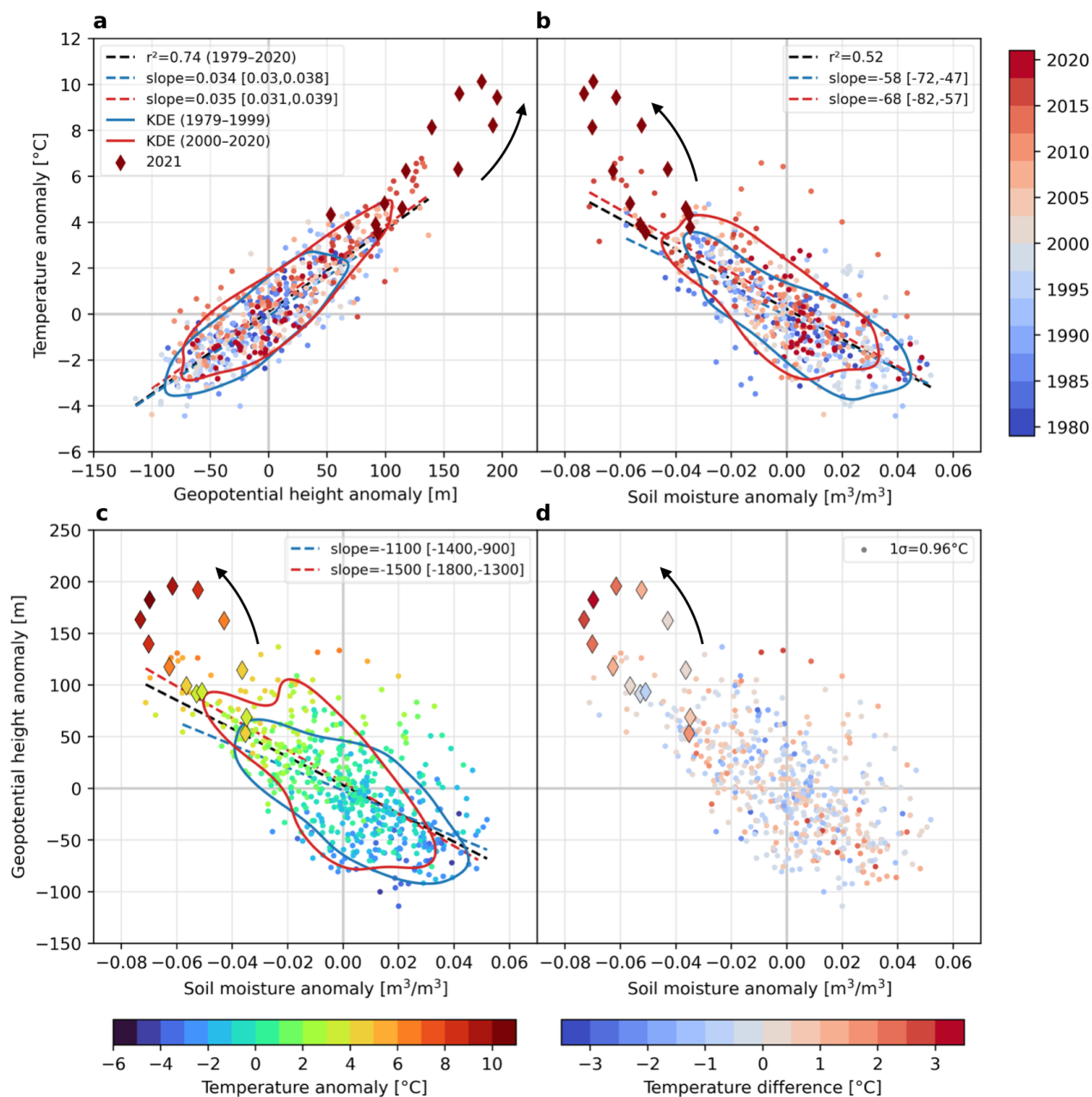
#### 84 **Unprecedented PNW heat conditions and contributing factors**

85 In ERA5 reanalysis (see Methods), anomalous near-surface temperatures during the PNW  
86 heatwave were accompanied by extremely high geopotential height and exceptionally low soil  
87 moisture. The regionally-averaged 2-meter temperature anomaly over land exceeded 5 times its  
88 daily standard deviation over 1981–2010, while geopotential height and soil dryness anomalies  
89 exceeded 4 and 3 of theirs (Fig. 1d). The PNW experienced at least seven days exceeding the  
90 99th percentile (over 1981–2010) in each of these variables (Fig. S1). However, this analysis of a  
91 large region (40–60°N, 130–110°W), capturing the broad-scale meteorological factors  
92 influencing the event rather than focusing on its most severe hotspots, this analysis may  
93 understate local severity: in some areas, 9-day-averaged (June 25–July 3) temperature exceeded  
94 12°C above normal.

95 The PNW was not the only anomalously hot region during this period: a hemisphere-  
96 wide pattern of anomalies extended from the land surface into the mid-atmosphere (Fig. 1a–c).  
97 Central Eurasia and northeastern Siberia both experienced warm anomalies, dry soils and high  
98 geopotential heights; the North Atlantic constituted a fourth high-geopotential-height region.  
99 With alternating cool, wet, and low-height regions, this pattern comprised a circumglobal  
100 wavenumber-4 disturbance (four peaks and troughs in each variable encircling the hemisphere;  
101 see Extended Data Fig. 1 for further details), a pattern historically associated with North  
102 American wildfires<sup>39</sup>. A wavenumber-4 upper-atmospheric circulation anomaly (see Methods)  
103 was established since June 19 (before the heatwave), and strongly amplified ( $>1.5\sigma$ ) since June  
104 21 (Fig. 1d, Extended Data Fig. 1). Accordingly, in late June the jet stream assumed a persistent  
105 “wavy” configuration with strong meridional wind meanders (Extended data Fig. 1, Fig. S2)—  
106 exhibiting a zonal-mean wind and temperature fingerprint for amplified planetary-scale waves  
107 that some evidence suggests may become more frequent with warming<sup>25,26,40</sup>. Further,  
108 convection in the western subtropical Pacific may have helped excite a late-June Rossby

109 wavetrain extending towards North America that locked phase with the existing hemispheric  
110 wave, amplifying the PNW's geopotential height and temperature anomalies and perhaps also  
111 strengthening the hemispheric wave (Extended Data Fig. 1), suggesting an important role for  
112 atmospheric dynamics in this event.

113         However, during the heatwave the PNW experienced markedly stronger temperature and  
114 height anomalies than other nodes of the hemispheric wave, despite similar soil moisture  
115 anomalies (compare Fig. 1b and 1c). Additionally, regional temperature continued rising during  
116 the event after geopotential height had peaked, mirroring the direction of soil moisture anomalies  
117 (Fig. 1d, Fig. S1). These observations suggest a potential role for both shorter-term atmospheric  
118 dynamics (Neal et al.<sup>41</sup> reveal an important contribution from upstream cyclogenesis leading to  
119 sudden blocking-induced heating aloft) and two-way land–atmosphere feedbacks in amplifying  
120 and prolonging the PNW heatwave.



121 **Fig. 2: Nonlinear interactions of common drivers and their long-term trends. a):** 3-day  
 122 running means of PNW-mean 2m temperature versus 500hPa geopotential height anomalies,  
 123 centered on each day from June 23–July 5 1979–2020, colored by year. Dark red diamonds  
 124 show 2021 (temperature maximizing on June 30); the arrow indicates their temporal evolution.  
 125 The historical linear regression between the variables is in black. Red and blue dashed lines  
 126 show regressions over 1979–1999 and 2000–2020 with 95% confidence intervals provided in  
 127 legends. Red and blue curves illustrate the 0.5 contour of a kernel density estimate (KDE) of the  
 128 variables' 2-dimensional distribution for each of the periods. **b–c):** same as **a)** for soil moisture  
 129 versus temperature anomalies and geopotential height anomalies; markers in **c)** are colored by  
 130 temperature anomaly. **d):** same as **c)** but dots colored by the difference between the observed  
 131 (colors in **c)** and predicted temperature for each soil moisture and geopotential height value

132 *pair (by multiple linear regression; see Fig. S3), indicating that the event's highest temperatures*  
133 *involved nonlinear contributions of  $\sim 3^{\circ}\text{C}$  out of a total  $\sim 10^{\circ}\text{C}$  anomaly.*  
134

### 135 **Nonlinear heat contributions from land–atmosphere interactions**

136 Interactions in the land–atmosphere system likely intensified the heatwave, contributing to a  
137  $\sim 3^{\circ}\text{C}$  nonlinear component (of the total  $\sim 10^{\circ}\text{C}$  peak regional-mean heat anomaly) above the heat  
138 accounted for by linear relations between driver variables (Fig. 2). The heatwave's proximate  
139 causes were extreme anomalies in common heatwave drivers—high geopotential height  
140 (resulting from wave-wave interaction; Extended Data Fig. 1), and dry soil, which both exceeded  
141 their historical (1979–2020) ranges yet largely followed expected bivariate distribution  
142 relationships (Fig. 2a–c), as in simulated record-shattering heatwaves in similar regions<sup>15</sup>.  
143 However, the heatwave's peak temperatures markedly exceeded temperature's linear regressions  
144 against geopotential height or soil moisture (by  $4\text{--}5^{\circ}\text{C}$ ), which are otherwise strongly predictive  
145 (Fig. 2a–b). A multiple regression, incorporating their simultaneous anomalies, confirms  
146 nonlinear temperature amplification maximizing during the event's peak at  $\sim 3^{\circ}\text{C}$  (i.e., increasing  
147  $\sim 7^{\circ}\text{C}$  by  $\sim 40\%$ ), a  $\sim 3\sigma$  amplification (Fig. 2c–d). Temporally, this amplification term behaved  
148 out-of-phase with geopotential height but in-phase with soil moisture (it increased as soils  
149 continued to dry despite declining geopotential height; Fig. 2d, Fig. 1d, Fig. S4), raising the  
150 possibility that two-way soil moisture–temperature interactions contributed to these  
151 nonlinearities.

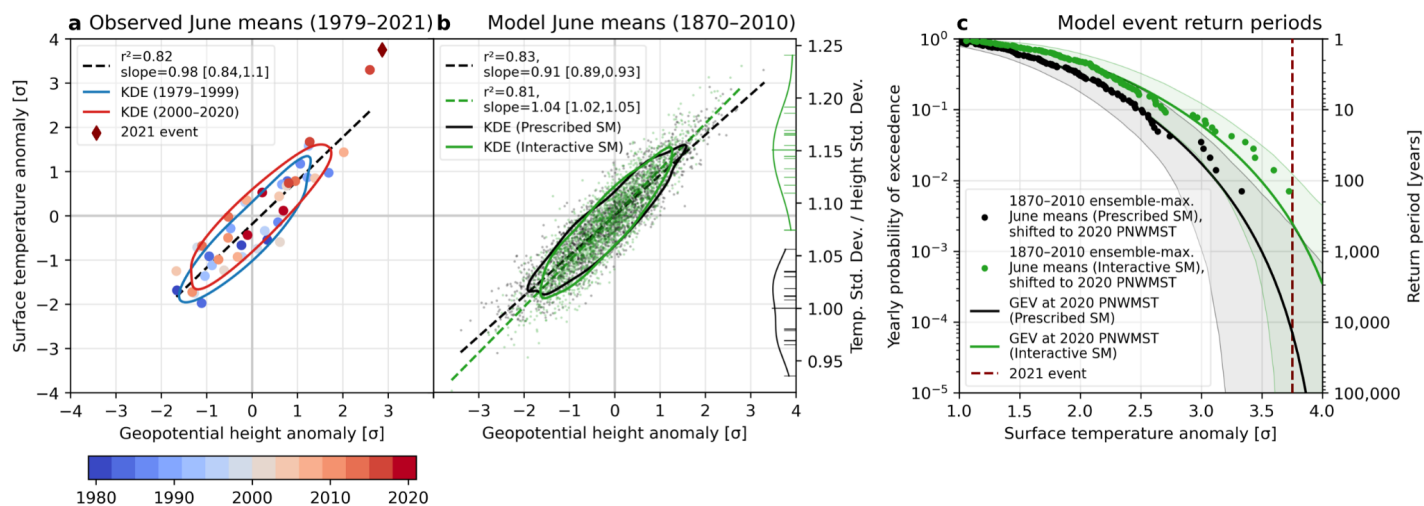
152 From a spatial perspective, dryness across much of the region following a beginning-June  
153 heatwave persisted throughout June, even during cool periods, establishing potential  
154 preconditions for land-atmosphere feedbacks (Fig. S5; Fig. 1d). Ultimately, many of the event's  
155 highest temperature anomalies were collocated with negative evaporative fraction anomalies  
156 (most notably in the region's interior plateaus, across eastern Washington and central British  
157 Columbia; warmer areas with more arid and Mediterranean continental climates), their  
158 convergence suggesting a region of potential feedback activity (Extended Data Fig. 2). We find  
159 that enhanced sensible and suppressed latent heat fluxes extended across many parts of the  
160 region, and tended to correspond with increased warming relative to available radiative energy  
161 versus areas with different flux partitioning (Extended Data Fig. 3, Extended Data Fig. 4). More  
162 quantitatively, an 850hPa-level temperature budget reveals distinct evolutions and drivers of  
163 heating within different sub-regions (Extended Data Fig. 5). For example, adiabatic compression



164 and horizontal advection contributed strongly to heating along British Columbia’s coastal ranges  
165 and immediately west of the Cascades, partially triggered by an offshore cut-off low pressure  
166 system. However, overall, the budget’s residual term (which estimates diabatic heating, likely  
167 related in part to land–atmosphere processes) provided heating during the heatwave’s peak  
168 warming days, and was ultimately the dominant driver in areas where 2-meter temperature  
169 anomalies became most extreme—in the region’s interior, as the heatwave progressed eastward.  
170 This substantiates that, in addition to other processes, land–atmosphere interactions likely  
171 amplified the heating, especially where and when it was strongest (Extended Data Fig. 5), though  
172 further analysis is needed to link 850hPa-level behavior directly to surface processes.  
173 Meanwhile, many of the most extreme areas that plausibly experienced land–atmosphere  
174 temperature amplification have experienced multidecadal summer drying, warming, and  
175 temperature variability increases (Extended Data Fig. 6; see Conclusions).

176         Furthermore, ongoing trends favor the nonlinear regional-mean behavior amplifying this  
177 heatwave—thus while 2021’s extreme heat was unprecedented, it was nevertheless  
178 mechanistically linked to historical regional climate change. First, the driver variables’  
179 distributions have individually shifted towards 2021’s conditions: late-June–early-July  
180 temperature, geopotential height, and soil dryness increased over 1979–2020, with trends  
181 accelerating over 1991–2020 (Figs. S6, S7). Consequently, the largest historical extremes in  
182 these variables tend to occupy more recent years (Fig. 2a–b). Second, bivariate distributions  
183 combining these variables have shifted towards high temperature and geopotential height and dry  
184 soils occurring simultaneously (Fig. 2a–b, visually comparing kernel density estimate [KDE]  
185 contours). Notably, historical extreme temperatures approaching 2021 conditions have also  
186 tended to be displaced above the linear driver regressions (Fig. 2a–b). Indeed, while bivariate  
187 distribution shifts have primarily followed their underlying regressions, the slopes describing the  
188 temperature and geopotential height relationships with soil moisture have strengthened (with  
189 probability 71% and 98%, respectively, via bootstrapping), indicating magnified temperature and  
190 geopotential height anomalies relative to soil moisture anomalies (Fig. 2b–c). Temperature–  
191 height density contours also potentially suggest a changing relationship in the distribution’s  
192 positive extremes, despite the unchanging linear relation (Fig. 2a), suggesting a change specific  
193 to heatwave mechanisms. While these conclusions hold over all of June–July (Fig. S4), we note

194 that late-June–early-July has exhibited especially pronounced trends in these variables and their  
195 variabilities (Fig. S7), perhaps reflecting an advancing summer onset<sup>43</sup>.



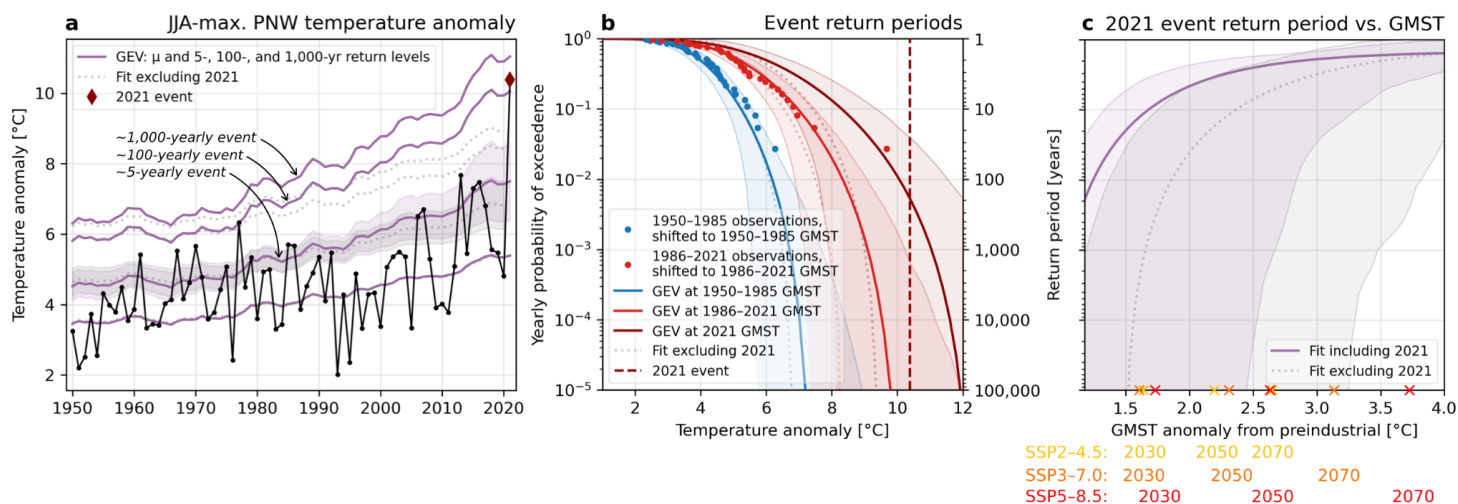
196 **Fig. 3: Modeled PNW monthly temperature variability and extreme event return periods, with**  
 197 **versus without soil moisture interaction.** June-mean PNW-mean surface temperature versus  
 198 500hPa geopotential height anomalies (standardized), from **a)** reanalysis (1979–2021) and **b)**  
 199 the CAM5–GOGA model experiment (1870–2010), comparing Prescribed (black) versus  
 200 Interactive (green) soil moisture ensembles. Regressions and KDE contours are as in Fig. 3 (but  
 201 with 1.25x smoothing in **a)** and showing the 0.3 contour in **b)**). **b)** also compares (right y-axis)  
 202 the ratio of each member’s geopotential height standard deviation to the Prescribed ensemble-  
 203 total temperature standard deviation. Longer lines show ensemble-total ratios; curves show  
 204 KDEs. **c)** shows exceedance probability and return period as a function of standardized  
 205 temperature anomaly for GEV distributions (curves) fit to 1870–2010 ensemble-maximum June  
 206 means and empirical return periods (dots). The estimated return period for the June 2021  
 207 temperature anomaly ( $\sim 3.75\sigma$ ) is  $\sim 35$ -fold shorter ( $\sim 400$ -yearly vs.  $\sim 14,000$ -yearly) with  
 208 interactive soil moisture.

### 210 Role of soil moisture in amplifying PNW temperature extremes

211 Using a model experiment tailored to evaluate the role of soil moisture in climate, we determine  
 212 that in the PNW, soil moisture–atmosphere interactions likely make monthly-scale temperature  
 213 extremes of June 2021’s magnitude many times more probable. We force a climate model with  
 214 historical (1870–2010) sea surface temperatures, both with and without soil moisture  
 215 interactivity (hereafter, Interactive and Prescribed ensembles), and we compare June-mean  
 216 surface temperature model output with observations (2-meter temperature was not available). We  
 217 first confirm that the observed June-mean 2021 surface temperature was extreme (Fig. 4a), with  
 218 monthly temperature reaching  $\sim 3.75\sigma$  and exceeding its regression against geopotential height.  
 219 In the model (standardized for comparison with observations; see Methods), we find that soil  
 220 moisture interaction significantly increases the ratio of monthly temperature variability versus  
 221 geopotential height variability between ensembles in total (by 15%), and across all members

222 individually (Fig. 4b, right axis). Consistent with previous research<sup>44</sup>, temperature variability  
223 increases modestly in Interactive members, accompanying strongly increased mean temperature  
224 (Fig. S8). Accordingly, the height–temperature regression slope across all member-months is  
225 significantly steeper in Interactive (by 14%), while both lie within the confidence interval of the  
226 observed slope (Fig. 4b, left axis). However, this linear slope increase may underestimate  
227 changes toward the distributions’ tails, i.e. during extremes (Fig. 4b, KDE contours).

228         Consequently, the likelihood of June 2021’s standardized temperature anomaly  
229 significantly increases when soil moisture interacts with the atmosphere. Generalized Extreme  
230 Value (GEV) distributions are fit to each ensemble’s yearly ensemble-maximum June-mean  
231 temperature anomaly (see Methods), and their location parameters are nonstationary in 5-year-  
232 smoothed annual PNW-mean surface temperature (PNWMST). We use PNWMST as a covariate  
233 to account for differing PNW mean climate responses to global temperature between model  
234 configurations. Estimated empirical return periods are overlaid on the model curves, with each  
235 observation shifted by the GEVs’ location parameter dependence on PNWMST. Fits and  
236 observations for each ensemble can thus be compared at a consistent baseline: at 2020’s  
237 PNWMST the GEV models estimate a ~35-fold increase (95% CI: 0.07–700,000) in the  
238 likelihood of 2021’s observed monthly anomaly between Prescribed and Interactive SM  
239 ensembles, transforming from an extremely unlikely ~15,000-year (440–∞) event to a ~410-year  
240 (80–∞) event. Overlaid empirical return periods suggest that GEV-derived return periods may  
241 conservatively estimate particularly severe events. Qualitatively similar results are found if two-  
242 or three-year GEV block sizes are used, or if all JJA months are used instead of just June (not  
243 shown).



244 **Fig. 4: 2021 heatwave likelihood estimates over recent decades and under future emissions**  
 245 **pathways. a):** A GEV distribution fit to yearly June–August (JJA)-maximum daily-mean PNW-  
 246 mean 2m temperature overlaid on observations, both including (purple) and excluding (gray  
 247 dotted) 2021’s event, plotting the location parameter ( $\mu$ ) and 5-, 100-, and 1000-year  
 248 period temperature levels (5-year return level bootstrapped 95% confidence interval shaded). **b):**  
 249 return periods of temperature anomalies for historical periods 1950–1985 and 1986–2021 (fits  
 250 are evaluated at and observations are shifted to the period-mean GMSTs), and for 2021 (finding  
 251 a ~200-yr return period). **c):** GEV fits evaluated as a function of GMST, providing likelihood  
 252 estimates for a future analogous event under different emission pathways (CMIP6 multimodel-  
 253 mean warming trajectories are displayed for reference). Future probabilities far exceed those  
 254 estimated until today: the event may become a 10-yearly event before 2050 in even an  
 255 intermediate emissions scenario (SSP2-4.5).  
 256

### 257 Increasing event likelihood driven by climate change

258 Recent climate change has rapidly increased the likelihood of the 2021 heatwave: over the past  
 259 70 years, such an event has multiplied in probability from virtually impossible to a multi-  
 260 hundred-year event (Fig. 5). As above, we apply GEV analysis, a targeted approach for  
 261 estimating extreme value statistics and an established method for attributing climate extremes to  
 262 anthropogenic warming<sup>45–47</sup>. We note that assessing the probability of this event in temperature  
 263 alone—despite its multivariate extreme characteristics—likely conservatively estimates its  
 264 increasing likelihood as a compound event, given simultaneous trends in other variables such as  
 265 soil moisture.

266 First, we note that the PNW has experienced not only shifting mean temperatures but also  
 267 changing variability since 1979: daily-mean June–July temperature anomalies have displayed  
 268 positive and increasing skewness both regionally-averaged (Fig. S10) and across many within-

269 region areas (Extended Data Fig. 6). While station-based daily-maximum and -minimum  
270 temperatures during July–August have shown small skewness in the PNW and not displayed  
271 strong historical increases<sup>48</sup>, here we highlight an earlier summer period and daily-mean  
272 temperatures. We further note that research has projected future modeled temperature skewness  
273 increases under CO<sub>2</sub> forcing in the PNW, likely linked to soil moisture interaction<sup>49</sup>.

274 We apply GEV analysis to yearly-maximum June–August (JJA) daily temperatures  
275 extending back to 1950, to maximize sample size and robustness, with both location and scale  
276 parameters nonstationary in 5-year-smoothed global mean surface temperature (GMST; see  
277 Methods; stationary scale parameter results are shown in Extended Data Fig. 7). Results reveal  
278 drastic historical changes in heatwave probabilities: a hypothetical daily 8°C regional  
279 temperature anomaly is estimated to have been virtually impossible in the 1950–1985 climate,  
280 but has become a ~50-year event in the climate since 1986 (Fig. 5b). Similarly, the 2021  
281 heatwave (a ~10.4°C peak anomaly, far exceeding the historical range) was virtually impossible  
282 even at the average global temperature over 1986–2021 (return period 95% CI: 1,500–∞), but by  
283 2021 has become a ~200-year event (25–∞)—thereby experiencing an infinite increase in  
284 probability (at least ~13-fold). Its probability increase since 1950–1985 is likewise infinite (at  
285 least ~500,000-fold). Furthermore, the probability of an event exceeding 2021’s magnitude will  
286 increase rapidly under further-increasing GMST—projected to recur ~10-yearly before 2050  
287 even at the warming of SSP2-4.5, a ‘moderate’ emissions scenario (before 2070 if excluding  
288 2021 from the fit; Fig. 5c).

289 Fig. 5 shows GEV fits both including 2021’s heatwave as well as excluding it. In  
290 including 2021, we follow Van Oldenborgh et al.<sup>46</sup> and Philip et al.<sup>47,50</sup>, assuming 2021’s  
291 observation is drawn from the same distribution as historical observations, since the study region  
292 was not selected solely to maximize local extremity but rather for a large-scale regional  
293 perspective, reducing (but not eliminating) selection bias. The excluding-2021 fit estimates a  
294 finite maximum possible temperature well below the 2021 observation even under current  
295 warming (Fig. 5b), questioning its validity. We note that the including-2021 fit is not rejected by  
296 a Kolmogorov-Smirnov test (Fig. S9) despite its poor fit in similar analyses<sup>47,50</sup>, which  
297 maintained a fixed scale parameter and analyzed a smaller region more concentrated on the  
298 extreme. Ultimately, both fits underscore dramatic increases in heat extreme probabilities  
299 resulting from gradual warming: in both, a ~1,000-year event in the 1950s would currently

300 resemble a ~5-year event, and has been surpassed multiple times (Fig. 5a). Furthermore,  
301 comparing future projections of a 2021-magnitude event, the fits roughly converge, both  
302 projecting <10-yearly recurrences by 2.5°C GMST above preindustrial. This threshold only  
303 increases to 2.75°C GMST in a fit with stationary instead of nonstationary scale parameter  
304 (Extended Data Fig. 7).

**305 Conclusions**

306 Given the 2021 heatwave's extreme magnitude, an important question is whether it represents a  
307 black swan event<sup>17,18</sup>, effectively unforeseeable no matter the climate conditions; a grey swan  
308 event<sup>19</sup>, made plausible by linking to common drivers and even more likely by background  
309 warming; or further, an event whose drivers do not act stationarily with respect to a moving  
310 background climate but are instead mechanistically altered by climate trends—with event  
311 likelihood thereby increasing beyond that induced by a background shift. We first find that,  
312 although 2021's event was unprecedented by large margins, it was traceable to common drivers,  
313 exhibiting extreme anomalies<sup>15</sup>. Interacting circulation features provided highly anomalous  
314 atmospheric dynamical forcing ( $4\sigma$  geopotential height exceedance), and land–atmosphere  
315 feedbacks likely amplified the event's severity, contributing to a ~40% nonlinear amplification.  
316 Further, however, we also find that the interactions amplifying this heatwave are mechanistically  
317 linked to trends in temperature, soil moisture, and geopotential height increasing their likelihood,  
318 possibly suggesting a long-term shift in feedback behavior underway in the region compounding  
319 background warming.

320 In contrast to first assessments<sup>50</sup> who concluded that the atmosphere dynamical patterns  
321 during this extreme were likely not exceptional, we provide evidence that the interaction of a  
322 persistent anomalous wavenumber-4 Rossby wave in the Polar front jet and an atmospheric wave  
323 emanating from the Pacific likely played a key role in this extraordinary temperature anomaly  
324 (Fig. 1, Extended Data Fig. 1). Further research is required to assess if the conditions for such  
325 waves are becoming more likely, e.g. by strengthened waveguidability<sup>51</sup> of the Polar front jet due  
326 to amplified land warming at high latitudes<sup>52,53</sup> or increased convective activity in the tropical  
327 pacific.

328 Warming-forced midlatitude land drying<sup>35,36</sup> could shift wet regions, such as much of the  
329 PNW, towards a transitional climate between wet and dry, possibly strengthening land-  
330 atmosphere feedbacks and temperature variability<sup>33</sup>. However, the PNW has received little  
331 examination of shifting soil moisture–temperature coupling, despite that some PNW areas  
332 already occupy transitional regimes during summer<sup>54,55</sup> and dry soil–heatwave linkages in the  
333 region are recognized<sup>56</sup>. Our findings suggest that rapid soil drying (particularly in early July,  
334 drying ~7% regionally between 1979–1999 and 2000–2020; Extended Data Fig. 6) may already  
335 be altering extreme heat mechanisms: many of the 2021 heatwave's anomalously hottest



336 temperatures occurred in areas experiencing long-term decreasing evaporative fraction and  
337 increasing temperature variability (Extended Data Fig. 2, Extended Data Fig. 6). We additionally  
338 find increasing trends in four metrics of the terrestrial component of land–atmosphere coupling  
339 in many of the same areas since 1979 (Extended Data Fig. 6). Notably, land-atmosphere  
340 coupling and temperature variability increases are strongest where soil moisture is  
341 climatologically moderate instead of the driest areas—thus in the PNW, drying may increase  
342 temperature variability more than in already-arid regions like the southwestern US<sup>33</sup>. In  
343 accordance with recent research demonstrating the emergence of heat-amplifying land–  
344 atmosphere feedbacks in regions not historically experiencing them<sup>32</sup> and, moreover, projections  
345 of widespread midcentury soil moisture regime shifts including the PNW<sup>37</sup>, we suggest that the  
346 2021 heatwave may represent an alarming manifestation of a shifting regime across much of the  
347 PNW from wet to transitional climate, making such events more likely through strengthened soil  
348 moisture–temperature coupling—however, further research is required to substantiate this.

349 Our results underscore that even gradual warming over recent decades dramatically  
350 transformed the character of this event. Since 1950, an anomaly of this magnitude has been  
351 refigured from virtually impossible to plausible and somewhat expected, with a hundreds-of-  
352 years return period. Continued warming will cause the probability of an equal or stronger event  
353 to rapidly increase, potentially becoming a ~10-year occurrence with 2°C warming above  
354 preindustrial, potentially by 2050 in even a ‘moderate’ emissions scenario.

355 **Methods**

356

357 **Reanalysis data**

358 All reanalysis data are provided by ECMWF's ERA5<sup>57</sup>, obtained at  $\sim 0.25^\circ$  and 6-hourly  
359 resolution; all analyses involve daily or longer means.

360

361 **Model data**

362 The model experiment we present in Fig. 3b–c is referred to as CAM5–GOGA<sup>58,59</sup>. The  
363 atmospheric model is CAM5 (National Center for Atmospheric Research [NCAR] Community  
364 Atmosphere Model, version 5.3), which is the atmospheric component of the Community Earth  
365 System Model, version 1.2<sup>60</sup>, at T42 spectral ( $\sim 2.75^\circ$ ) resolution. The GOGA (Global Ocean  
366 Global Atmosphere) experiment involves forcing 16 members of CAM5 with historical monthly  
367 sea surface temperatures (HadISSTv2<sup>61</sup>) over the period 1856–2014. Greenhouse gasses (GHGs)  
368 and radiative forcing are fixed (GHGs at 2000 levels), and sea ice concentration follows  
369 HadISSTv2. One 16-member ensemble allows soil moisture to interact with the atmospheric  
370 model, while the other prescribes soil moisture as the monthly climatology over 1950–2015 at  
371 each location derived from all members. We begin analysis in 1870 to avoid model spin-up  
372 effects, and discard two full members and all years after 2010 due to data discrepancies, resulting  
373 in a 14-member by two-ensemble by 141-year dataset. For comparison with reanalysis, we  
374 standardize all anomalies, based on the whole period for all grouped Prescribed members, for  
375 model data, and based on the 1981–2010 climatology for reanalysis data. We note a caveat that  
376 in this experimental design, water is not strictly conserved in the Prescribed SM case, as noted  
377 for GLACE-CMIP5 models<sup>44,62,63</sup>—however, an analysis of the resulting water balance  
378 perturbation in the CESM model<sup>62</sup> shows the perturbation is small in the PNW relative to other  
379 global regions.

380 Future GMST trajectories in Fig. 4c are based on decadal-mean CMIP6 multimodel mean  
381 anomalies from the preindustrial period (1850–1900), using all models available (42 for SSP2-  
382 4.5, 35 for SSP3-7.0, and 44 for SSP5-8.5<sup>64</sup>).

383

384 **Planetary wave analysis**

385 We apply a Fourier transform to 15-day running means of 300hPa meridional wind averaged  
386 over 37.5–52.5°N, obtaining amplitudes and phase positions of the circulation components of  
387 zonal wavenumbers  $k=1-9$ . Amplitudes are compared with a monthly climatology over 1981–  
388 2010 to calculate standardized anomalies.

389

### 390 **Extreme value analysis**

391 Our estimates of likelihoods and return periods of extreme temperatures are derived by fitting  
392 Generalized Extreme Value (GEV) distributions to both observational (ERA5) and model data,  
393 following widely-used procedures designed for investigating extreme events rather than the body  
394 of distributions<sup>45–47,50,65</sup>. For all GEV analysis we use the Python package *climextRemes*<sup>66</sup>.

395 For observations, we first calculate the maximum daily-mean PNW-mean temperature  
396 anomaly over June–August (JJA) each year since 1950 using the ERA5 back extension<sup>67</sup>. We fit  
397 a GEV function with nonstationary location and scale parameters to both datasets 1950–2020  
398 and 1950–2021. Both nonstationary parameters use 5-year smoothed annual-mean GMST as a  
399 covariate, provided by NASA’s GISTEMP<sup>68</sup>. For both datasets, the addition of nonstationarity in  
400 the scale parameter improves the model fit over a stationary-scale fit, based on a Likelihood  
401 Ratio Test (significant at the  $p<0.025$  level for the 1950–2021 dataset, and with  $p=0.267$  for  
402 1950–2020; Table S1), and on comparing Kolmogorov-Smirnov test statistics (Fig. S9, Extended  
403 Data Fig. 7). A comparison of the GEV fits against empirical temperature return periods in  
404 1950–1985 vs. 1986–2021 visually supports a potential widening (Fig. 4b, Fig. S9). Moreover,  
405 as such nonstationarity would reflect a variability change rather than a mean shift, it may be  
406 physically justified by observed increases in regional temperature skewness since 1979,  
407 particularly in June (Extended Data Fig. 6, Fig. S10). The shape parameter, however, is kept  
408 stationary: it corresponds to the shape of the GEV’s upper tail, and a negative value (as found)  
409 indicates a fixed upper bound determining the highest temperature anomaly possible at a given  
410 global temperature, which is likely to be true based on energetic constraints.

411 For model data, we calculate the maximum June mean among all 14 ensemble members  
412 for each year. We fit a GEV to these ensemble-maximum June means over 1870–2010, with  
413 nonstationary location parameter using 5-year smoothed annual PNWMST as a covariate.  
414 Nonstationarity in GMST does not significantly improve the fits over total stationarity, while  
415 nonstationarity in PNWMST does ( $p<0.1$  and  $p<0.001$  for Prescribed and Interactive SM

416 ensembles, respectively). Fits are presented in Fig. 3 evaluated at 2020's annual PNWMST  
417 (calculated from ERA5) to provide present-day estimates of the 2021 event return periods  
418 without including its information in the PNWMST itself. We repeat the analysis with block size  
419 of 28 and 36 member-years (maxima over 2 and 3 years of data, respectively) and find fairly  
420 consistent results but with drastically increased uncertainty as the total block number decreases.

421 For all GEV results, 95% confidence intervals surrounding return period curves are  
422 shown based on a bootstrapping method, as a non-parametric alternative to a parametric method  
423 using asymptotic standard errors. Bootstrapping is done with a block size of one year, and is  
424 obtained by resampling (drawing  $n$  out of a given  $n$  datapoints with replacement, for 5,000  
425 iterations for model data and 1,000 iterations for observational data) and calculating the desired  
426 output (i.e., return periods as a function of return level) for each iteration. The displayed 95%  
427 confidence interval bounds are taken as the 2.5th and 97.5th percentiles of the resulting return  
428 period curves. (Bootstrapping in Fig. 2 is also done with a one-year block size and 5,000  
429 iterations.)

430

### 431 **Acknowledgements**

432 We are thankful to Yutian Wu, Radley Horton, Deepti Singh, Colin Raymond, Cassandra  
433 Rogers, and Richard Seager for valuable feedback on this work. We thank Donna Lee for  
434 configuring, running, and making output available from CAM5–GOGA. Support for this work  
435 was provided by NSF-AGS-1934358.

436

### 437 **Data Availability**

438 All ERA5 output used in this study is available from ECMWF at  
439 <https://cds.climate.copernicus.eu/cdsapp#!/dataset/reanalysis-era5-single-levels>. All  
440 CAM5\_GOGA output used in this study is available at <https://doi.org/10.5281/zenodo.5800726>.  
441 CMIP6 multimodel mean warming levels are available at  
442 <https://doi.org/10.5281/zenodo.4600695>.

443

### 444 **Code Availability**

445 All figures were produced using Python v.3.6  
446 (<https://www.python.org/downloads/release/python-360/>). All code needed to reproduce the  
447 main figures is available at [https://github.com/sambartusek/pnw\\_hw\\_2021](https://github.com/sambartusek/pnw_hw_2021).

448 **References**

- 449 1. Popovich, N. & Choi-Schagrin, W. Hidden Toll of the Northwest Heat Wave: Hundreds of  
450 Extra Deaths. *The New York Times* (2021).
- 451 2. Excess Deaths Associated with COVID-19.  
452 [https://www.cdc.gov/nchs/nvss/vsrr/covid19/excess\\_deaths.htm](https://www.cdc.gov/nchs/nvss/vsrr/covid19/excess_deaths.htm) (2021).
- 453 3. Coroners. [No title]. [https://www2.gov.bc.ca/gov/content/life-events/death/coroners-](https://www2.gov.bc.ca/gov/content/life-events/death/coroners-service/news-and-updates/heat-related)  
454 [service/news-and-updates/heat-related](https://www2.gov.bc.ca/gov/content/life-events/death/coroners-service/news-and-updates/heat-related).
- 455 4. Schramm, P. J. *et al.* Heat-Related Emergency Department Visits During the Northwestern  
456 Heat Wave - United States, June 2021. *MMWR Morb. Mortal. Wkly. Rep.* **70**, 1020–1021  
457 (2021).
- 458 5. US Census Bureau. American Housing Survey (AHS). [https://www.census.gov/programs-](https://www.census.gov/programs-surveys/ahs.html)  
459 [surveys/ahs.html](https://www.census.gov/programs-surveys/ahs.html).
- 460 6. Tigchelaar, M., Battisti, D. S. & Spector, J. T. Work Adaptations Insufficient to Address  
461 Growing Heat Risk for U.S. Agricultural Workers. *Environ. Res. Lett.* **15**, (2020).
- 462 7. US Drought Monitor Map Archive. <https://droughtmonitor.unl.edu/Maps/MapArchive.aspx>.
- 463 8. National Fire News. <https://www.nifc.gov/fire-information/nfn>.
- 464 9. Silverman, H., Guy, M. & Sutton, J. Western wildfire smoke is contributing to New York  
465 City’s worst air quality in 15 years. *CNN* (2021).
- 466 10. Meehl, G. A. & Tebaldi, C. More intense, more frequent, and longer lasting heat waves in  
467 the 21st century. *Science* **305**, 994–997 (2004).
- 468 11. Perkins-Kirkpatrick, S. E. & Lewis, S. C. Increasing trends in regional heatwaves. *Nat.*  
469 *Commun.* **11**, 3357 (2020).
- 470 12. Philip, S. Y. *et al.* Rapid attribution analysis of the extraordinary heatwave on the Pacific

- 471 Coast. [https://www.worldweatherattribution.org/wp-content/uploads/NW-US-extreme-heat-](https://www.worldweatherattribution.org/wp-content/uploads/NW-US-extreme-heat-2021-scientific-report-WWA.pdf)  
472 [2021-scientific-report-WWA.pdf](https://www.worldweatherattribution.org/wp-content/uploads/NW-US-extreme-heat-2021-scientific-report-WWA.pdf).
- 473 13. Coumou, D. & Robinson, A. Historic and future increase in the global land area affected by  
474 monthly heat extremes. *Environ. Res. Lett.* **8**, 034018 (2013).
- 475 14. Power, S. B. & Delage, F. P. D. Setting and smashing extreme temperature records over the  
476 coming century. *Nat. Clim. Chang.* **9**, 529–534 (2019).
- 477 15. Fischer, E. M., Sippel, S. & Knutti, R. Increasing probability of record-shattering climate  
478 extremes. *Nat. Clim. Chang.* **11**, 689–695 (2021).
- 479 16. Thompson, V. *et al.* The 2021 western North America heat wave among the most extreme  
480 events ever recorded globally. *Sci Adv* **8**, eabm6860 (2022).
- 481 17. Taleb, N. N. *The Black Swan: The Impact of the Highly Improbable*. (Random House  
482 Publishing Group, 2007).
- 483 18. Aven, T. On the meaning of a black swan in a risk context. *Saf. Sci.* **57**, 44–51 (2013).
- 484 19. Lin, N. & Emanuel, K. Grey swan tropical cyclones. *Nat. Clim. Chang.* **6**, 106–111 (2015).
- 485 20. Petoukhov, V., Rahmstorf, S., Petri, S. & Schellnhuber, H. J. Quasiresonant amplification  
486 of planetary waves and recent Northern Hemisphere weather extremes. *Proc. Natl. Acad.*  
487 *Sci. U. S. A.* **110**, 5336–5341 (2013).
- 488 21. Petoukhov, V. *et al.* Role of quasiresonant planetary wave dynamics in recent boreal spring-  
489 to-autumn extreme events. *Proc. Natl. Acad. Sci. U. S. A.* **113**, 6862–6867 (2016).
- 490 22. Screen, J. A. & Simmonds, I. Amplified mid-latitude planetary waves favour particular  
491 regional weather extremes. *Nat. Clim. Chang.* **4**, 704–709 (2014).
- 492 23. Kornhuber, K. *et al.* Summertime Planetary Wave Resonance in the Northern and Southern  
493 Hemispheres. *J. Clim.* **30**, 6133–6150 (2017).

- 494 24. Kornhuber, K. *et al.* Amplified Rossby waves enhance risk of concurrent heatwaves in  
495 major breadbasket regions. *Nat. Clim. Chang.* **10**, 48–53 (2019).
- 496 25. Mann, M. E. *et al.* Influence of Anthropogenic Climate Change on Planetary Wave  
497 Resonance and Extreme Weather Events. *Sci. Rep.* **7**, 45242 (2017).
- 498 26. Mann, M. E. *et al.* Projected changes in persistent extreme summer weather events: The role  
499 of quasi-resonant amplification. *Sci Adv* **4**, eaat3272 (2018).
- 500 27. Kornhuber, K. & Tamarin-Brodsky, T. Future changes in northern hemisphere summer  
501 weather persistence linked to projected arctic warming. *Geophys. Res. Lett.* **48**, (2021).
- 502 28. Hirschi, M. *et al.* Observational evidence for soil-moisture impact on hot extremes in  
503 southeastern Europe. *Nat. Geosci.* **4**, 17–21 (2010).
- 504 29. Miralles, D. G., van den Berg, M. J., Teuling, A. J. & de Jeu, R. A. M. Soil moisture-  
505 temperature coupling: A multiscale observational analysis. *Geophys. Res. Lett.* **39**, (2012).
- 506 30. Miralles, D. G., Teuling, A. J., van Heerwaarden, C. C. & Vilà-Guerau de Arellano, J.  
507 Mega-heatwave temperatures due to combined soil desiccation and atmospheric heat  
508 accumulation. *Nat. Geosci.* **7**, 345–349 (2014).
- 509 31. Rasmijn, L. M. *et al.* Future equivalent of 2010 Russian heatwave intensified by weakening  
510 soil moisture constraints. *Nat. Clim. Chang.* **8**, 381–385 (2018).
- 511 32. Dirmeyer, P. A., Balsamo, G., Blyth, E. M., Morrison, R. & Cooper, H. M. Land-  
512 atmosphere interactions exacerbated the drought and heatwave over northern Europe during  
513 summer 2018. *AGU Advances* **2**, (2021).
- 514 33. Seneviratne, S. I. *et al.* Investigating soil moisture–climate interactions in a changing  
515 climate: A review. *Earth-Sci. Rev.* **99**, 125–161 (2010).
- 516 34. Koster, R. D. *et al.* Regions of strong coupling between soil moisture and precipitation.



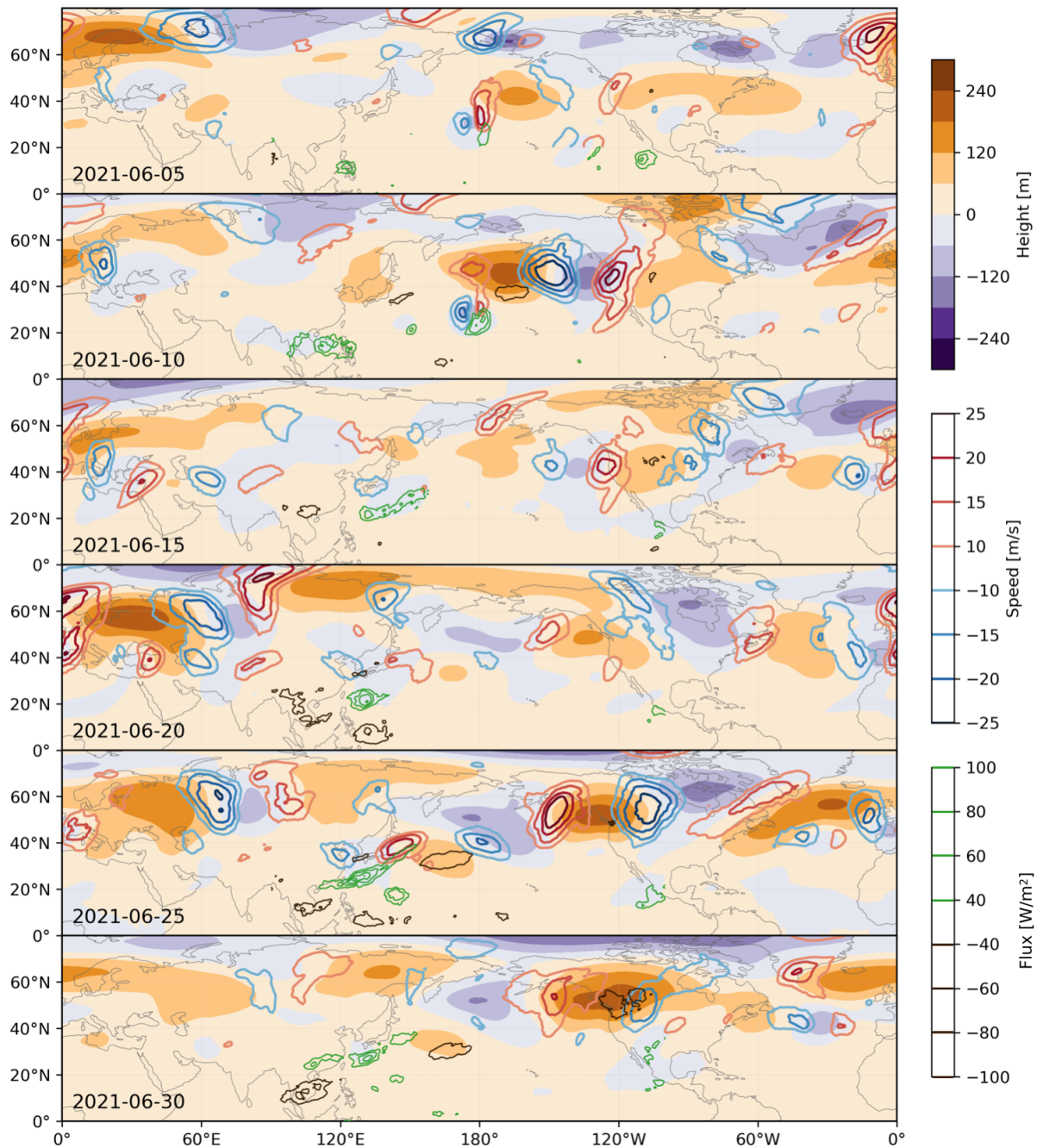
- 517        *Science* **305**, 1138–1140 (2004).
- 518    35. Cook, B. I., Smerdon, J. E., Seager, R. & Coats, S. Global warming and 21st century  
519        drying. *Clim. Dyn.* **43**, 2607–2627 (2014).
- 520    36. Cook, B. I., Ault, T. R. & Smerdon, J. E. Unprecedented 21st century drought risk in the  
521        American Southwest and Central Plains. *Sci Adv* **1**, e1400082 (2015).
- 522    37. Dirmeyer, P. A. *et al.* Projections of the shifting envelope of Water cycle variability. *Clim.*  
523        *Change* **136**, 587–600 (2016).
- 524    38. Seneviratne, S. I., Lüthi, D., Litschi, M. & Schär, C. Land-atmosphere coupling and climate  
525        change in Europe. *Nature* **443**, 205–209 (2006).
- 526    39. Petoukhov, V. *et al.* Alberta wildfire 2016: Apt contribution from anomalous planetary  
527        wave dynamics. *Sci. Rep.* **8**, 12375 (2018).
- 528    40. Teng, H. & Branstator, G. Amplification of Waveguide Teleconnections in the Boreal  
529        Summer. *Current Climate Change Reports* **5**, 421–432 (2019).
- 530    41. Neal, E., Huang, C. S. Y. & Nakamura, N. The 2021 pacific northwest heat wave and  
531        associated blocking: Meteorology and the role of an upstream cyclone as a diabatic source  
532        of wave activity. *Geophys. Res. Lett.* **49**, (2022).
- 533    42. Schumacher, D. L. *et al.* Amplification of mega-heatwaves through heat torrents fuelled by  
534        upwind drought. *Nat. Geosci.* **12**, 712–717 (2019).
- 535    43. Wang, J. *et al.* Changing lengths of the Four Seasons by global warming. *Geophys. Res.*  
536        *Lett.* **48**, (2021).
- 537    44. Berg, A. *et al.* Impact of Soil Moisture–Atmosphere Interactions on Surface Temperature  
538        Distribution. *J. Clim.* **27**, 7976–7993 (2014).
- 539    45. Swain, D. L., Singh, D., Touma, D. & Diffenbaugh, N. S. Attributing Extreme Events to

- 540 Climate Change: A New Frontier in a Warming World. *One Earth* **2**, 522–527 (2020).
- 541 46. van Oldenborgh, G. J. *et al.* Pathways and pitfalls in extreme event attribution. *Clim.*  
542 *Change* **166**, 13 (2021).
- 543 47. Philip, S. *et al.* A protocol for probabilistic extreme event attribution analyses. *Advances in*  
544 *Statistical Climatology, Meteorology and Oceanography* vol. 6 177–203 (2020).
- 545 48. McKinnon, K. A., Rhines, A., Tingley, M. P. & Huybers, P. The changing shape of  
546 Northern Hemisphere summer temperature distributions. *J. Geophys. Res.* **121**, 8849–8868  
547 (2016).
- 548 49. Volodin, E. M. & Yurova, A. Y. Summer temperature standard deviation, skewness and  
549 strong positive temperature anomalies in the present day climate and under global warming  
550 conditions. *Clim. Dyn.* **40**, 1387–1398 (2013).
- 551 50. Philip, S. Y. *et al.* Rapid attribution analysis of the extraordinary heatwave on the Pacific  
552 Coast of the US and Canada June 2021. *Earth Syst. Dyn.* 1–34 (2021) doi:10.5194/esd-  
553 2021-90.
- 554 51. White, R. H., Kornhuber, K., Martius, O. & Wirth, V. From Atmospheric Waves to  
555 Heatwaves: A Waveguide Perspective for Understanding and Predicting Concurrent,  
556 Persistent and Extreme Extratropical Weather. *Bull. Am. Meteorol. Soc.* **-1**, 1–35 (2021).
- 557 52. Xu, P. *et al.* Amplified waveguide teleconnections along the polar front jet favor summer  
558 temperature extremes over northern Eurasia. *Geophys. Res. Lett.* **48**, (2021).
- 559 53. Liu, Y., Sun, C. & Li, J. The Boreal Summer Zonal Wavenumber-3 Trend Pattern and Its  
560 Connection with Surface Enhanced Warming. *Journal of Climate* vol. 35 833–850 (2022).
- 561 54. Dirmeyer, P. A. The terrestrial segment of soil moisture-climate coupling. *Geophys. Res.*  
562 *Lett.* **38**, (2011).

- 563 55. Schwingshackl, C., Hirschi, M. & Seneviratne, S. I. Quantifying Spatiotemporal Variations  
564 of Soil Moisture Control on Surface Energy Balance and Near-Surface Air Temperature. *J.*  
565 *Clim.* **30**, 7105–7124 (2017).
- 566 56. Mueller, B. & Seneviratne, S. I. Hot days induced by precipitation deficits at the global  
567 scale. *Proc. Natl. Acad. Sci. U. S. A.* **109**, 12398–12403 (2012).
- 568 57. Hersbach, H. *et al.* The ERA5 global reanalysis. *Quart. J. Roy. Meteor. Soc.* **146**, 1999–  
569 2049 (2020).
- 570 58. Lee, D. E., Ting, M., Vigaud, N., Kushnir, Y. & Barnston, A. G. Atlantic Multidecadal  
571 Variability as a Modulator of Precipitation Variability in the Southwest United States. *J.*  
572 *Clim.* **31**, 5525–5542 (2018).
- 573 59. Pomposi, C., Giannini, A., Kushnir, Y. & Lee, D. E. Understanding Pacific Ocean influence  
574 on interannual precipitation variability in the Sahel. *Geophys. Res. Lett.* **43**, 9234–9242  
575 (2016).
- 576 60. Neale, R. B. *et al.* The Mean Climate of the Community Atmosphere Model (CAM4) in  
577 Forced SST and Fully Coupled Experiments. *J. Clim.* **26**, 5150–5168 (2013).
- 578 61. Titchner, H. A. & Rayner, N. A. The Met Office Hadley Centre sea ice and sea surface  
579 temperature data set, version 2: 1. Sea ice concentrations. *J. Geophys. Res.* **119**, 2864–2889  
580 (2014).
- 581 62. Hauser, M., Orth, R. & Seneviratne, S. I. Investigating soil moisture-climate interactions  
582 with prescribed soil moisture experiments: an assessment with the Community Earth  
583 System Model (version 1.2). *Geosci. Model Dev. Discuss.* 1–18 (2016).
- 584 63. Humphrey, V. *et al.* Soil moisture–atmosphere feedback dominates land carbon uptake  
585 variability. *Nature* **592**, 65–69 (2021).

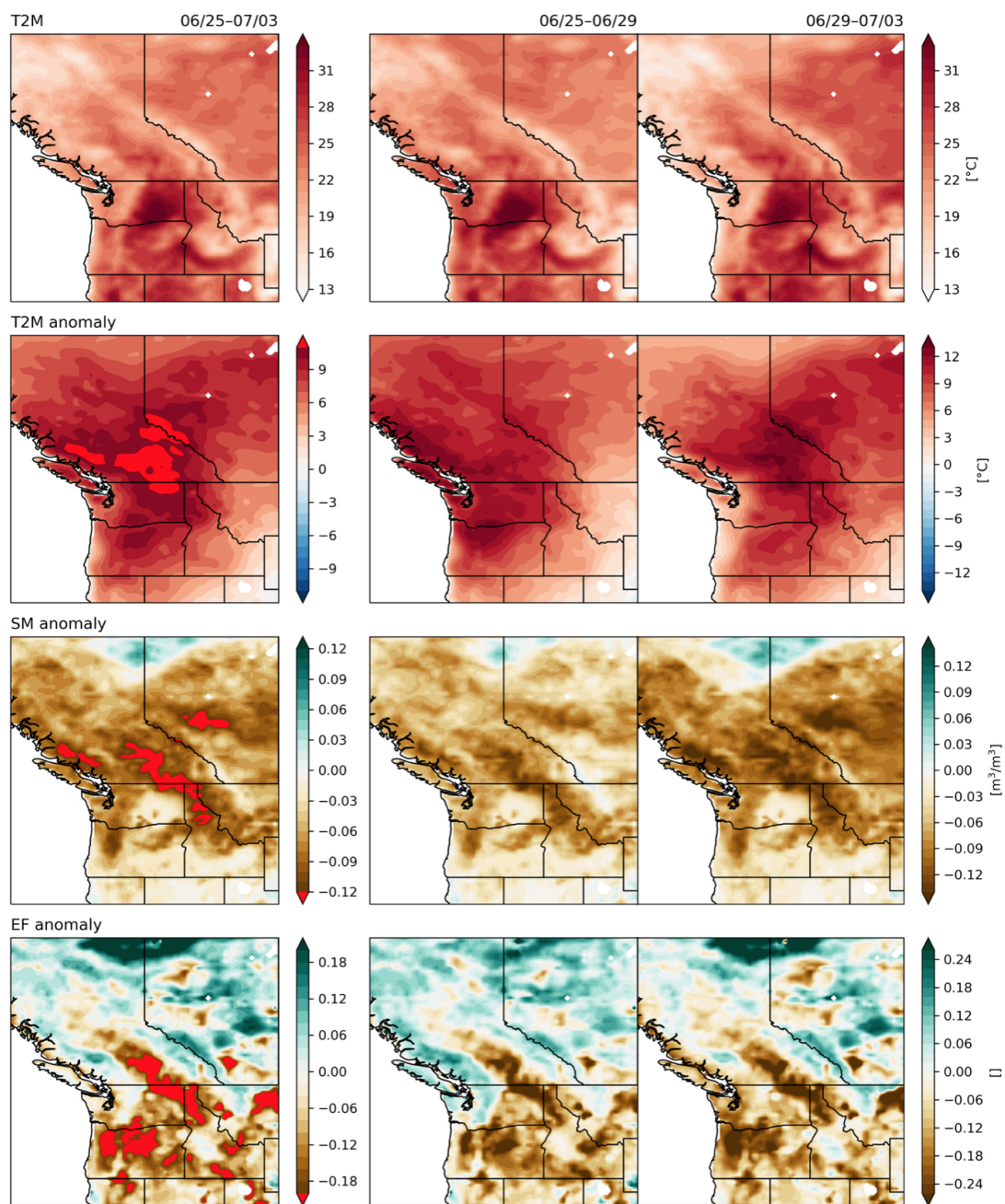
- 586 64. Hauser, M. *mathause/cmip\_temperatures: version 0.2.1.* (2021).  
587 doi:10.5281/zenodo.5532894.
- 588 65. Coles, S. *An Introduction to Statistical Modeling of Extreme Values.* (Springer, London,  
589 2001).
- 590 66. Paciorek, C. *climextRemes: Tools for Analyzing Climate Extremes.* (2019).  
591 doi:10.5281/zenodo.3240582.
- 592 67. Bell, B. *et al.* The ERA5 global reanalysis: Preliminary extension to 1950. *Quart. J. Roy.*  
593 *Meteor. Soc.* **147**, 4186–4227 (2021).
- 594 68. Data.GISS: GISS surface temperature analysis (GISTEMP v4).  
595 <https://data.giss.nasa.gov/gistemp/>.
- 596 69. Archambault, H. M., Bosart, L. F., Keyser, D. & Cordeira, J. M. A Climatological Analysis  
597 of the Extratropical Flow Response to Recurring Western North Pacific Tropical Cyclones.  
598 *Mon. Weather Rev.* **141**, 2325–2346 (2013).
- 599 70. Stuivenolt Allen, J., Simon Wang, S.-Y., LaPlante, M. D. & Yoon, J.-H. Three western  
600 pacific typhoons strengthened fire weather in the recent northwest U.s. conflagration.  
601 *Geophys. Res. Lett.* **48**, (2021).
- 602 71. Oey, L.-Y. & Chou, S. Evidence of rising and poleward shift of storm surge in western  
603 North Pacific in recent decades. *J. Geophys. Res. C: Oceans* **121**, 5181–5192 (2016).
- 604 72. Sharmila, S. & Walsh, K. J. E. Recent poleward shift of tropical cyclone formation linked to  
605 Hadley cell expansion. *Nat. Clim. Chang.* **8**, 730–736 (2018).
- 606 73. Wang, R. & Wu, L. Influence of Track Changes on the Poleward Shift of LMI Location of  
607 Western North Pacific Tropical Cyclones. *J. Clim.* **32**, 8437–8445 (2019).

608 **Extended Data Figures**



609 **Extended Data Fig. 1: Atmospheric dynamics during June 2021 leading to the anomalous**  
 610 **geopotential heights associated with the PNW heatwave.** See Text S1 for further discussion.  
 611 **a-f):** 500hPa Geopotential height (filled contours), 300hPa meridional wind speed (red and blue  
 612 contours), and outgoing longwave radiation (OLR; green and dark brown contours) anomalies  
 613 averaged over 9-day periods centered on the annotated date. For clarity, the meridional wind

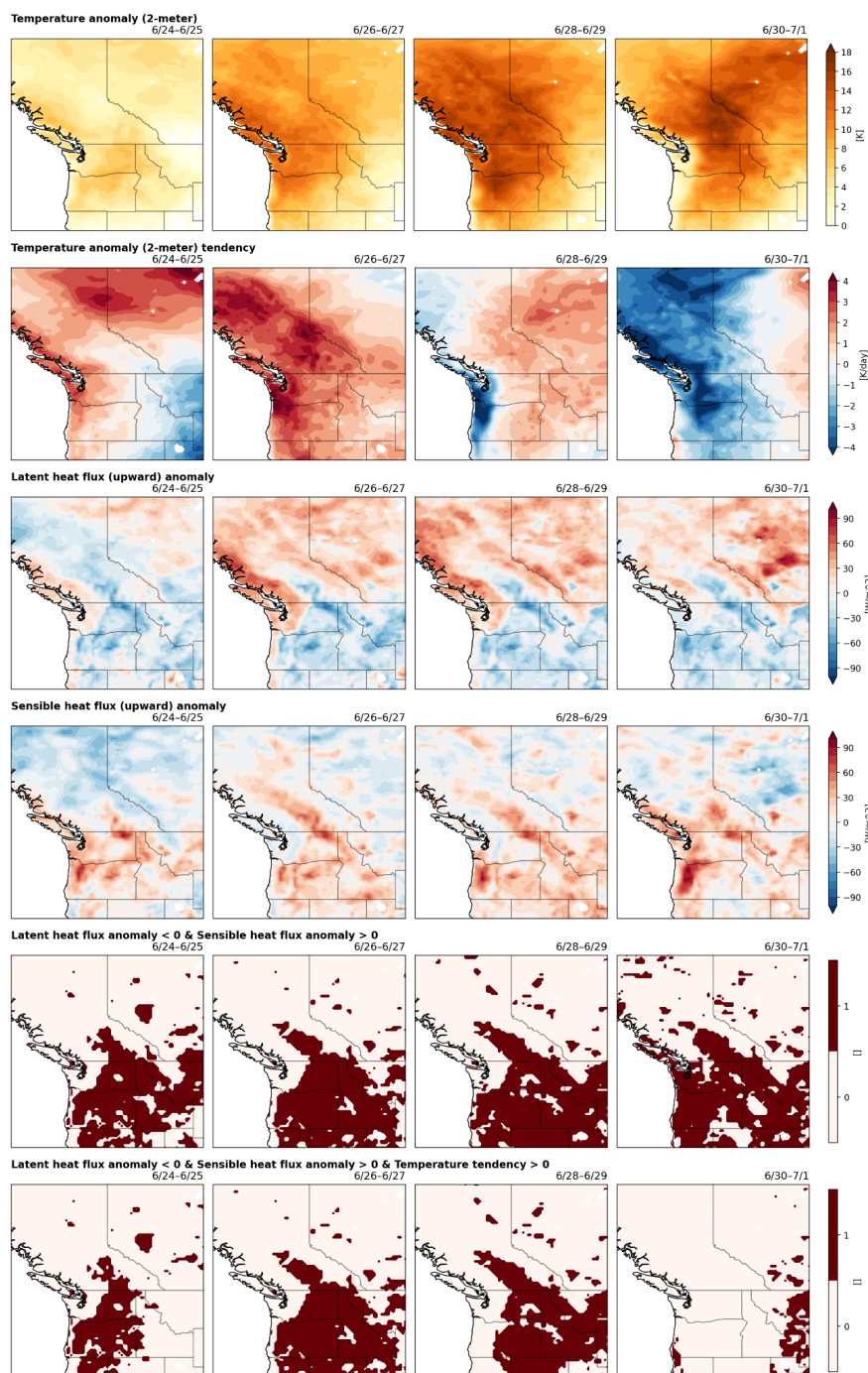
614 field is only shown poleward of 20°N and the OLR field is only shown within 90°E–100°W  
615 (roughly the Pacific Ocean). **a)** shows the 9-day mean surrounding 06/05, when geopotential  
616 heights were high in the PNW accompanying a heatwave, with centers of low and high  
617 geopotential height extending westward over the Pacific and forming a tripole. By 06/10 (**b)**) the  
618 tripole had expanded longitudinally, placing negative geopotential height over the PNW, and  
619 begun to constitute part of a wavenumber-4 pattern in meridional wind and geopotential height  
620 encircling the midlatitudes. Over 06/10–06/20 (**c–e**) this wavenumber-4 pattern moved slightly  
621 northward and shifted phase longitudinally, eventually placing high geopotential height over the  
622 PNW. Throughout the last two weeks of June (**d–f**) the wavenumber-4 pattern persisted and  
623 amplified, causing extreme temperatures and dry soils in central Europe, Siberia, and the PNW,  
624 and was reinforced by a Rossby wavetrain emanating from the subtropical western Pacific.



625 **Extended Data Fig. 2: PNW land-atmosphere anomalies during the 2021 heatwave.** Mean  
 626 conditions over the whole 9-day heatwave period (06/25–07/03; **left column**), its first half  
 627 (06/25–06/29; **middle column**), and its second half (06/29–07/03; **right column**), for 2m  
 628 temperature (T2M) (**top row**), T2M anomalies (**second row**), soil moisture (SM) anomalies  
 629 (**third row**), and evaporative fraction (EF) anomalies (**bottom row**). EF is calculated from  
 630 daily-mean latent heat flux (LHF) and sensible heat flux (SHF) as  $LHF/(SHF+LHF)$ . Many of

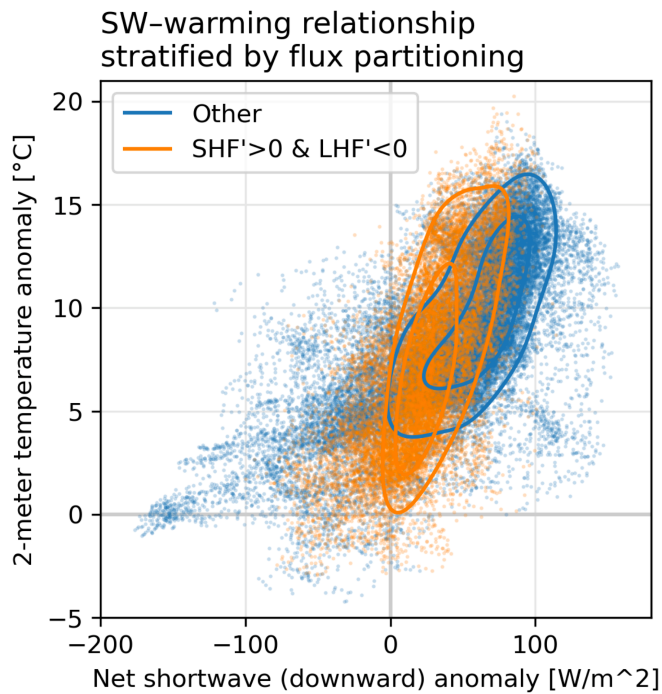
631 the regions of hottest (absolute) T2M and hottest T2M, driest SM, and lowest EF anomalies  
632 during this heatwave overlapped, particularly in the center of the region: across northern Oregon,  
633 eastern Washington, northern Idaho, and central southern British Columbia (the Interior Plateau).  
634 However, some of the largest T2M anomalies were associated with high EF anomalies instead—  
635 mostly in the Coastal and Cascade mountains on the British Columbia coast and the Cariboo and  
636 Monashee mountains between British Columbia and Alberta. This pattern is very consistent with  
637 climatological daily correlation between EF and T2M anomalies (see Extended Data Fig. 6):  
638 areas where EF and T2M are anti-correlated (both typically and during this event) tend to be  
639 warmer, non-mountain areas with relatively low soil moisture and more arid and/or  
640 Mediterranean continental climates (i.e., across much of eastern Oregon and Washington (the  
641 Columbia Plateau), Idaho, and British Columbia's Interior Plateau. Therefore, overall,  
642 throughout the heatwave (06/25–07/03), the spatial anti-correlation between EF and T2M  
643 anomalies was very weak, reflecting the diversity of land types and land-atmosphere coupling  
644 regimes across the large region (yielding  $r=-0.04$ ). However, where T2M was both anomalously  
645 and climatologically high, EF and T2M were more tightly anti-correlated. Masking to retain only  
646 land regions under the 850hPa level, the spatial correlation was  $-0.24$ , with  $p<0.0001$   
647 (significance tested non-parametrically, accounting for spatial autocorrelation).



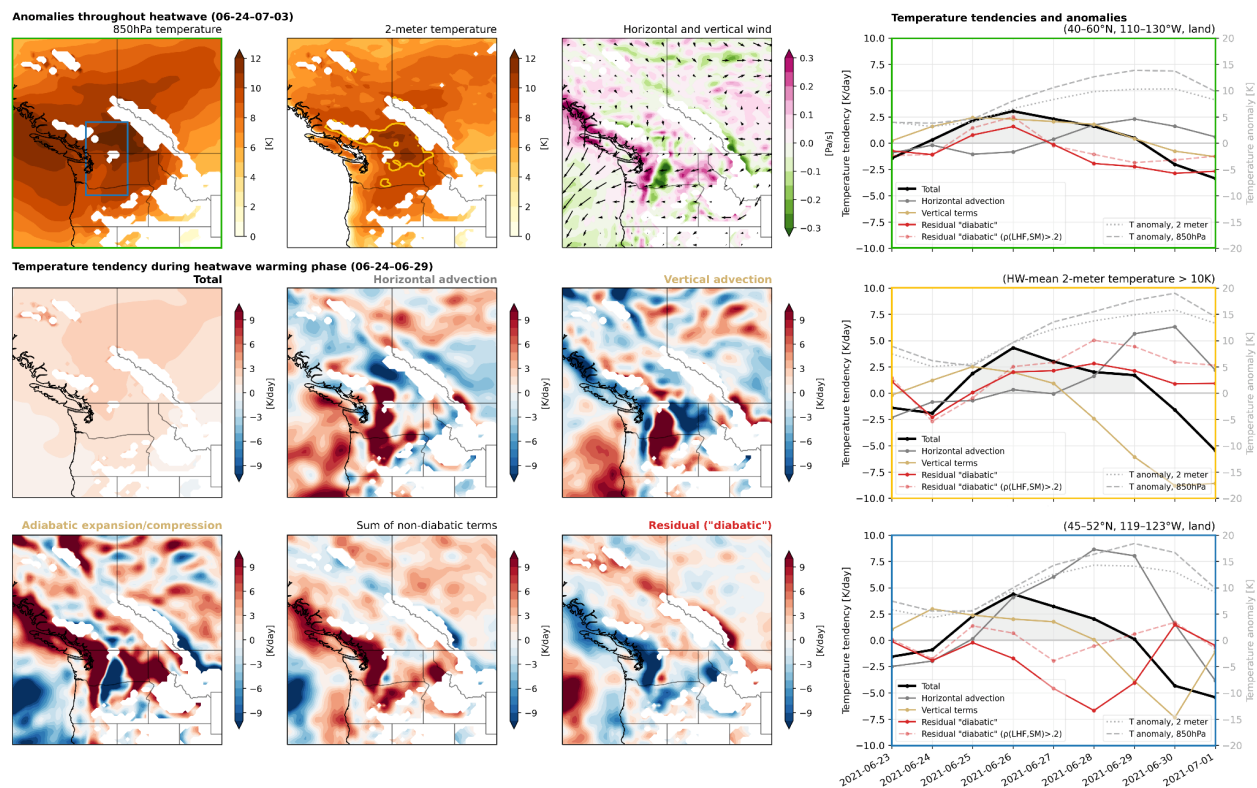


648 **Extended Data Fig. 3: 2-meter temperature anomaly, tendency, and latent versus sensible**  
 649 **heat flux partitioning.** Two-day averages throughout 6/24–7/1, focusing on the heating phase of  
 650 the event. The second-to-last row identifies points where the (upward) two-day average upward  
 651 latent heat flux (LHF) was diminished and sensible heat flux (SHF) was enhanced (exhibiting  
 652 negative and positive anomalies relative to 1981–2010, respectively, which tend to show strong

653 persistence throughout the season). The last row further subselects points where the temperature  
654 tendency was also positive.

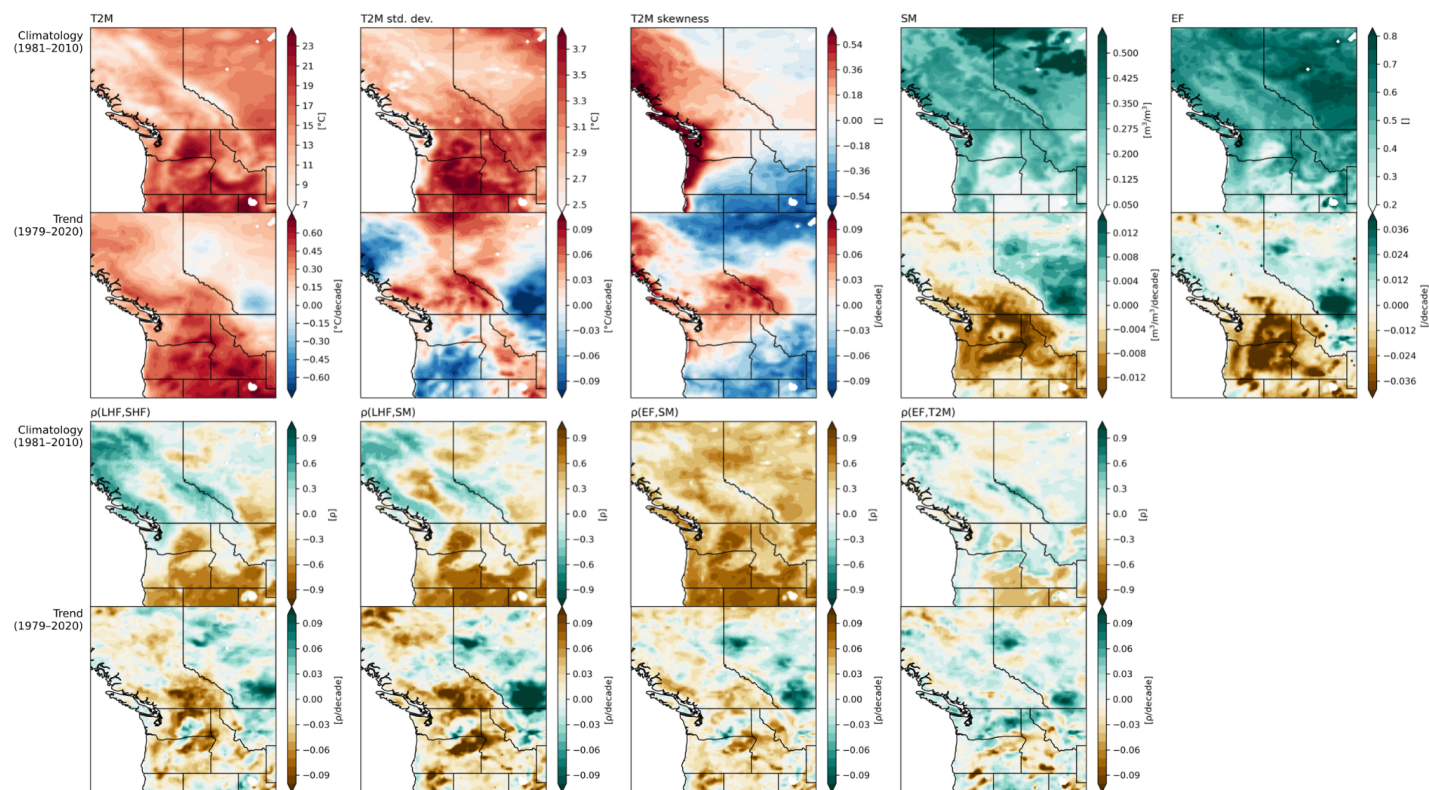


655 **Extended Data Fig. 4: SW-warming relationship stratified by flux partitioning.** Points are  
656 daily averages for each land gridcell in the PNW region, over the heatwave period (06/25–  
657 07/02), with net SW downward anomaly plotted against 2-meter temperature anomaly. Orange  
658 dots represent daily-averages at each point within the evolving mask shown in the second-to-last  
659 row of Extended Data Fig. 3, i.e. where (upward) sensible heat flux (SHF) was enhanced and  
660 latent heat flux (LHF) was diminished. Blue dots show all other land gridcells in the region.  
661 Kernel density estimate (KDE) contours are shown for each group of gridcells, considering only  
662 points with net anomalous shortwave radiation > 0, so that points not relevant to heating do not  
663 bias the KDE characterization.  
664



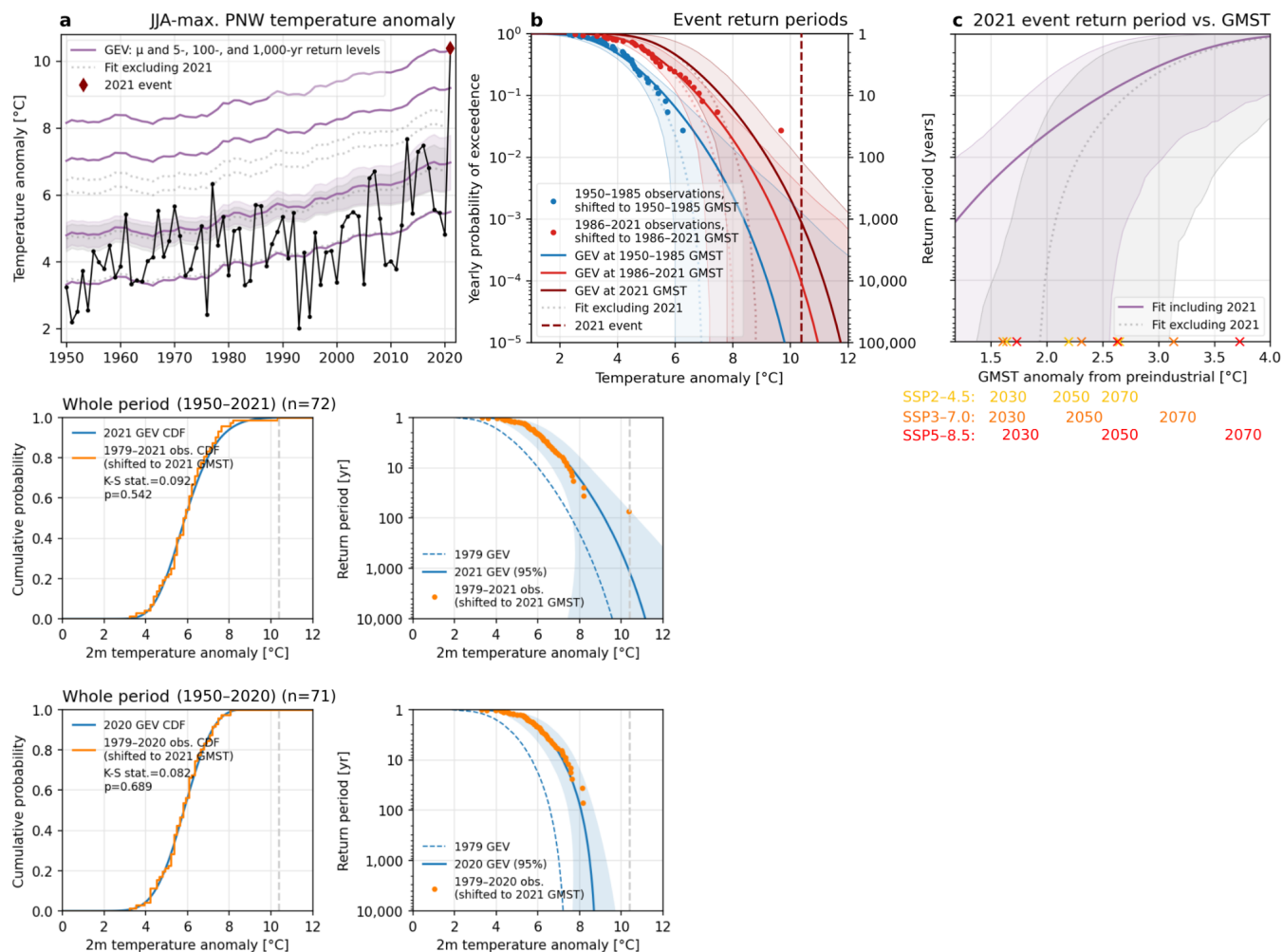
665 **Extended Data Fig. 5: Temperature tendency budget analysis at 850hPa.** See Text S2 for  
 666 further discussion. **Top row, left:** Temperature (at 850hPa and 2 meters) and horizontal and  
 667 vertical wind (at 850hPa) anomalies averaged during the heatwave (06/24–07/03). The green  
 668 box, blue box, and yellow contour outline the sub-regions highlighted in the right column (the  
 669 green box shows the region focused on in the manuscript). **Bottom two rows, left:** Spatial  
 670 patterns of contributions from various (grouped) terms in the 850hPa temperature tendency  
 671 budget, averaged throughout the heatwave warming phase (06/24–06/29). The residual  
 672 “diabatic” term is calculated as the total tendency minus the sum of all non-diabatic terms, and  
 673 indicates processes not accounted for by the non-diabatic terms that may in part be attributed to  
 674 land–atmosphere processes. Fields are smoothed with a running 4-gridcell ( $\sim 1^\circ$ ) window in both  
 675 directions. **Right column:** Temporal evolution of grouped terms in the budget throughout 06/23–  
 676 07/01, averaged within the green, yellow, and blue outlined areas (in top row of maps). Solid  
 677 lines show the total heating, horizontal heat advection, the sum of vertical heat advection and  
 678 adiabatic expansion/compression, and the residual term. Additionally, the dashed translucent red  
 679 line shows the residual term only where the long-term daily correlation between latent heat flux  
 680 (LHF) and soil moisture (SM) exceeds 0.2 (see Extended Data Fig. 6), i.e., where land–

681 atmosphere interactions may be more likely to cause positive feedbacks on temperature  
682 extremes. 2-meter and 850hPa temperature anomalies in each sub-region are shown on the right  
683 axes.



684 **Extended Data Fig. 6: Climatologies and trends of PNW temperature variability, land**  
 685 **surface quantities, and land-atmosphere coupling climatologies and trends. Top row: 1981–**  
 686 **2010 June–July climatologies (top panels) and 1979–2020 linear trends (bottom panels) of 2m**  
 687 **temperature (T2M), T2M variability, soil moisture (SM), and evaporative fraction (EF). T2M**  
 688 **standard deviation and skewness are intra-annual, measuring the within-year variability of daily**  
 689 **anomalies (taken from the 1981–2010 daily climatology). EF is calculated from daily latent heat**  
 690 **flux (LHF) and sensible heat flux (SHF) as  $LHF/(LHF+SHF)$ . Climatologies are calculated using**  
 691 **only 1981–2010 data. Trends consider 1979–2020 and are presented in per-decade units. Bottom**  
 692 **row: Climatologies and trends of four metrics of land-atmosphere coupling: correlations**  
 693 **between LHF and SHF, LHF and SM, EF and SM, and EF and T2M. At each gridpoint, a**  
 694 **correlation climatology is created by taking daily anomalies (from the daily 1981–2010**  
 695 **climatology) for each variable during June–July 1979–2020, removing their 1979–2020 linear**  
 696 **trends, and correlating two variables against each other throughout all June–July 1981–2010**  
 697 **days. Correlation trends are determined by calculating correlations within each year (June–July)**  
 698 **separately, and finding a linear trend in yearly correlation values over 1979–2020 at each**  
 699 **gridpoint. Results are consistent if trends are estimated by subtracting the correlation over 1979–**

1999 from that over 2000–2020. The first three correlations represent the terrestrial component of land-atmosphere coupling while  $\rho(\text{EF}, \text{T2M})$  represents the total feedback pathway. While SM and T2M are nearly everywhere anticorrelated, these correlations show where soil moisture deficit may causally affect T2M. Areas where LHF and SHF are anticorrelated, LHF and SM are correlated, EF and SM are correlated, and EF and T2M are anticorrelated indicate “moisture-limited” regimes with potentially stronger land-atmosphere coupling (as distinct from “energy-limited” regimes where the atmosphere dominantly controls land-surface processes). Such correlation directionalities are typical of “transitional” climate zones between wet and dry: in wet enough areas, soil moisture deficits do not affect evapotranspiration (near-zero  $\rho(\text{EF}, \text{SM})$ ) because a non-limited supply of moisture allows LHF to increase in response to atmospheric heating (positive  $\rho(\text{LHF}, \text{SHF})$  and negative  $\rho(\text{LHF}, \text{SM})$ )—conversely, if SM is lower, LHF is limited and thus EF (LHF’s proportion of total flux) decreases (positive  $\rho(\text{EF}, \text{SM})$  and  $\rho(\text{LHF}, \text{SM})$  and negative  $\rho(\text{LHF}, \text{SHF})$ ). In moisture-limited evapotranspiration areas, decreased EF (i.e., increased SHF partition of total flux) can raise T2M, allowing for positive land-atmosphere feedbacks as raised T2M can further decrease SM, increase SHF, decrease LHF, and decrease EF. Such areas climatologically extend from the drier interior central West, to the Columbia Plateau in eastern Washington, and even into the British Columbia Interior Plateau (bottom row, top panels). Trends over 1979–2020 indicate that much of the PNW is has undergone strengthening in at least the terrestrial component of land-atmosphere coupling— notably, mostly where soil moisture is climatologically moderate as opposed to extremely low (where further drying may instead decrease such correlations), which includes much of BC’s Interior Plateau, much of the Cascade Range region (including Portland and near Seattle) and to the east of the Columbia Plateau. Trends in  $\rho(\text{EF}, \text{T2M})$  indicate that in some of these areas (mostly in the southern PNW but including some of the BC Interior Plateau), T2M itself has become more coupled to EF, potentially signifying increased feedbacks—but overall, such trends have not conclusively emerged. The spatial pattern of trends toward stronger land-atmosphere coupling correspond relatively well with warming, drying SM, and decreasing EF, and in some places with increasing T2M variability: areas of increasing T2M standard deviation and skewness correspond better to land-atmosphere correlation trends than to SM or EF trends alone. (Increasing skewness is furthermore detectable at the regional level; see Fig. S10.)



730 **Extended Data Fig. 7: Fit and validation for nonstationary-location, stationary-scale**  
 731 **historical GEV fit. Top row:** Same as Fig. 4 but for the GEV fit with fixed scale parameter.  
 732 **Middle and bottom rows:** Model fit against empirical CDF and return periods, for the whole  
 733 period since 1950, with and without 2021. See Fig. S9 caption.



734 **Supplementary Information**

735

736 Supplementary Information file for “**2021 North American Heatwave Amplified by Climate-**  
737 **Change-Driven Nonlinear Interactions**”

738

739 Samuel Bartusek<sup>\*,1,2</sup>, Kai Kornhuber<sup>2,3</sup>, Mingfang Ting<sup>2</sup>

740 1. Department of Earth and Environmental Sciences, Columbia University, New York, NY,  
741 USA

742 2. Lamont-Doherty Earth Observatory, Columbia University, Palisades, NY, USA

743 3. German Council on Foreign Relations, DGAP, Berlin, Germany

744

745 \*Corresponding author: Samuel Bartusek, [samuel.bartusek@columbia.edu](mailto:samuel.bartusek@columbia.edu)

746

747

748 **Contents of this file:**

749

- 750 • Supplementary Text S1–2
- 751 • Supplementary Figures S1–10
- 752 • Supplementary Table S1

753 **Text S1: Anomalous geopotential heights fueled by the interaction of two distinct Rossby**  
754 **waves (Extended Data Fig. 1)**

755 Mutually-reinforcing slow- and fast-moving circulation features provided atmospheric dynamical  
756 forcing for the heatwave, each carrying potential climate linkages that may result in increased  
757 risk of concurrency and associated extreme impacts. First, the planetary wavenumber-4  
758 circulation anomaly persisted during much of June, producing synchronized climate extremes  
759 throughout the hemisphere, and dramatically amplified in late June boosting temperatures and  
760 drying soils in the PNW. Accordingly, in late June the jet assumed a persistent anomalous  
761 “wavy” configuration with strong meridional wind meanders (Fig. 2, Extended Data Fig. 1). Its  
762 northern excursions, encircling anticyclonic anomalies, formed an anomalous polar jet that  
763 together with the subtropical jet created a midlatitude waveguide, and zonal-mean temperature  
764 anomalies then peaked where zonal wind gradients were strongest ( $\sim 60^\circ\text{N}$ ; Extended Data Fig.  
765 1). These conditions represent a fingerprint for planetary wave amplification that some evidence  
766 suggests may become more frequent with warming, and may be connected to a weakening  
767 meridional temperature gradient<sup>25,26,40</sup>. Secondly, convection in the western subtropical Pacific  
768 (south of Japan) generated negative outgoing longwave radiation (OLR) anomalies, exciting a  
769 late-June Rossby wavetrain extending towards North America. This synoptic wavetrain locked  
770 phase with the existing hemispheric wave, amplifying the PNW’s geopotential height and  
771 temperature anomalies and perhaps also strengthening the hemispheric wave (Extended Data Fig.  
772 1). Recent findings show that typhoons undergoing extratropical transition south of Japan can  
773 heighten PNW wildfire risk by inducing downslope easterly winds across the Cascade Range  
774 that adiabatically warm and dry<sup>69,70</sup>, as demonstrated during 2021<sup>50</sup>. A projected northward shift  
775 in typhoon tracks in this region under global warming<sup>71–73</sup> could increase the risk of such events.

776 **Text S2: Temperature Budget Analysis (Extended Data Fig. 5)**

777 In Extended Data Fig. 5, we first (top row, maps) present a comparison of temperature anomalies  
778 averaged throughout the heatwave (06/24–07/03) at both 2 meters and 850hPa, which show  
779 similar geographical patterns with the most intense anomalies centered over interior British  
780 Columbia and eastern Washington. Horizontal and vertical wind anomalies at 850hPa are also  
781 shown, notably displaying easterly anomalies in Washington and Oregon, accompanied by  
782 ascent upwind of the Cascades and descent downwind. Given the complex topography in the  
783 region, we next perform a temperature budget analysis at the 850hPa level, using the  
784 methodology of He and Black (2016, Heat budget analysis of Northern Hemisphere high-latitude  
785 spring onset events, *J. Geophys. Res. Atmos.*, 121, 10,113–10,137, doi:10.1002/  
786 2015JD024681).

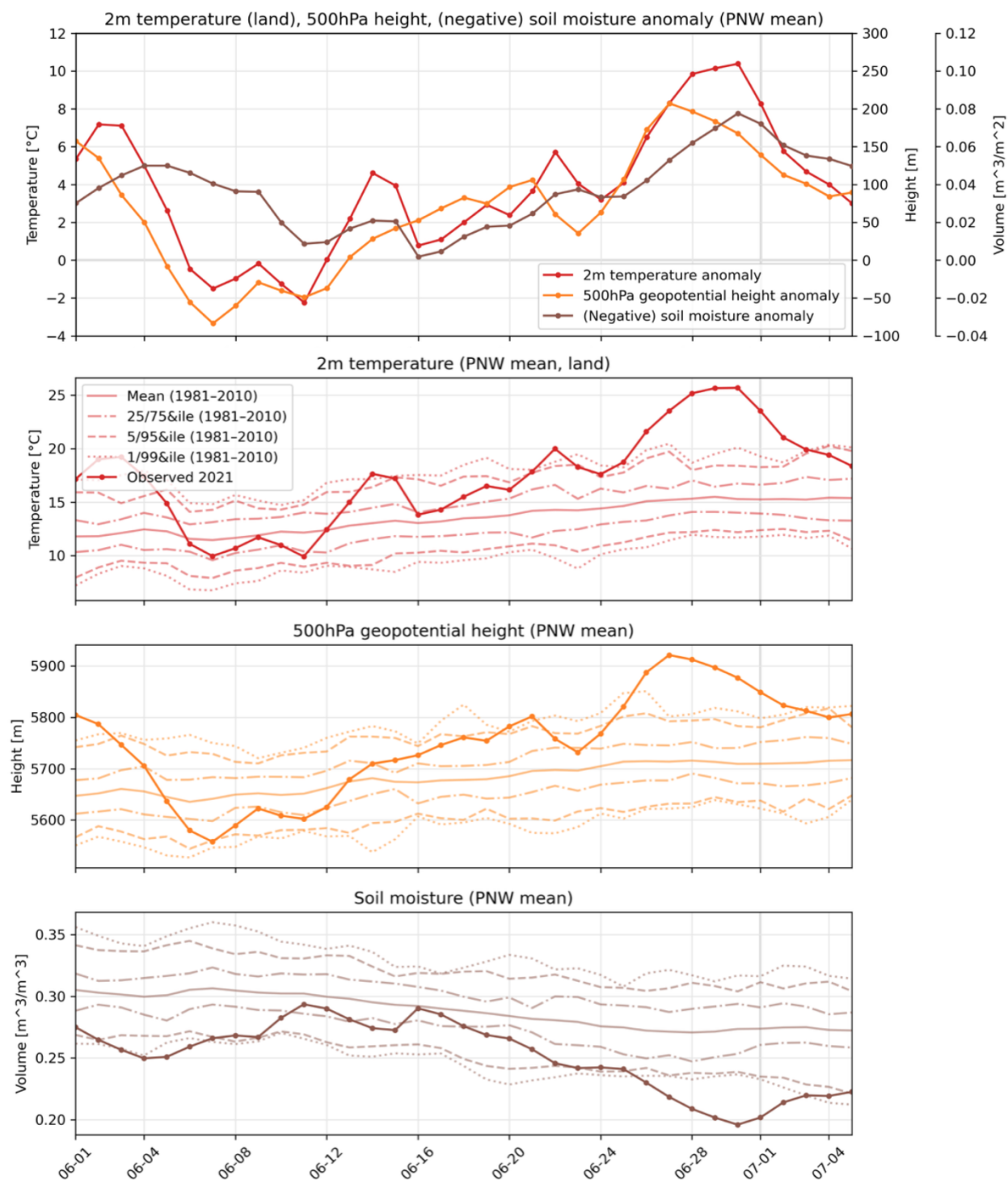
787 Overall, at the 850hPa level, we find heterogeneous patterns and strong canceling  
788 between large terms in the temperature budget equation (bottom two rows, maps). Throughout  
789 the heatwave warming period (06/24–06/29), horizontal advection clearly contributes to heating  
790 along and downwind of the Cascades but is opposed in many areas by vertical advection and  
791 adiabatic expansion/compression, and remains overall slightly negative in the interior British  
792 Columbia and eastern Washington plateau regions, where temperature anomalies were highest  
793 (both at 2 meters and 850hPa). Adiabatic compression and vertical advection strongly oppose  
794 each other in many areas, and when added to horizontal advection, heating is strong downwind  
795 of the Cascades and Northern Rockies and the immediate coastal mountains of British Columbia,  
796 but still near zero (and even negative in places) in the interior Plateaus of British Columbia and  
797 eastern Washington. Eddy terms (included in horizontal and vertical advection) are noisy (even  
798 at the smoothed spatial scale presented here, with a 4-grid-cell or  $\sim 1^\circ$  smoother) and contribute  
799 both heating and cooling. Altogether, a time-averaged “diabatic” term (estimated as a residual of  
800 all non-diabatic budget terms from the total temperature tendency) indicates that unaccounted-for  
801 diabatic processes may have been important to the total heating, notably in the interior British  
802 Columbia and Columbia Plateaus, where we have argued that EF and T anomaly correspondence  
803 and surface flux partitioning indicate potential feedback activity, and where temperature  
804 anomalies ultimately became most extreme.

805 A temporal view of some aggregated terms of the heat budget (right column) highlights  
806 the different progression and drivers of heating in different sub-regions within the PNW.

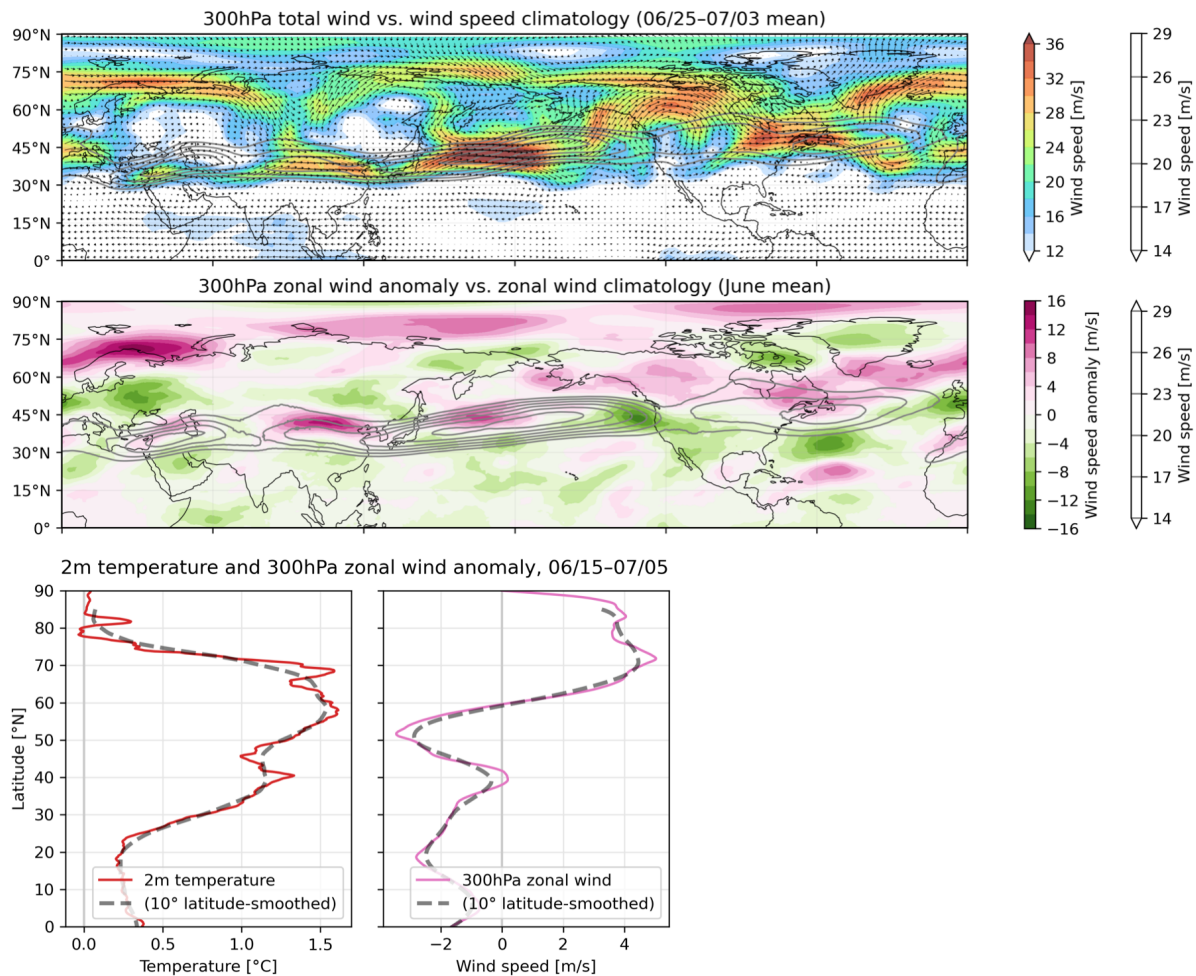
807 Averaged over the whole region (top panel, green outline in top left map), the net vertical terms  
808 provided strong warming (driven by the adiabatic term), partially canceled by horizontal  
809 advective cooling throughout most of the heatwave's warming phase. However, on the days of  
810 maximum heating, the residual term played a large warming role, providing above 50% of the  
811 net heating on the maximum day (06/27). It later became negative as the horizontal advection  
812 strengthened, and heating rate overall weakened. Subsetting for areas where historical latent heat  
813 flux and soil moisture correlation indicates that land-atmosphere feedbacks may be typical  
814 ( $\rho(\text{LHF}, \text{SM}) > 0.2$ , based on Extended Data Fig. 6's climatology), the residual term evolves very  
815 similarly and slightly strengthens, indicating that these areas may be especially responsible for  
816 the residual effects. In the sub-region of highest 2 meter temperature anomalies (middle panel,  
817 yellow outline in top center map), however, the diabatic term is more positive, ultimately  
818 providing the dominant contribution to the overall warming (and even stronger when masking  
819 for LHF/SM correlation). The term strengthens throughout the event, leading to the sub-region's  
820 anomalous warmth peaking one day later than that averaged across the whole region. (The  
821 diabatic term's positive influence here is therefore not fully reflected in the maps, which end on  
822 06/29). This demonstrates strong coincidence between the heatwave's most extreme areas (below  
823 850hPa) and areas of strongest potential land-atmosphere interactions as estimated by the  
824 diabatic term. Similar results are found where 850hPa heatwave-mean temperature exceeds  
825 12°C. Finally, we highlight a region where horizontal advective and adiabatic heating terms  
826 strongly dominate the budget (bottom panel, blue outline in top left map)—the Cascades and  
827 immediately to their west, in a corridor containing Portland and Seattle (45–52°N, 119–123°W,  
828 the region used by the WWA study and Thompson et al., *Sci Adv.*, 2022). Here, very strong  
829 easterlies triggered by an offshore cut-off low pressure system (whose signature is somewhat  
830 visible in the top right map, but strongest June 28th–29th) led to strong dynamics-driven heating  
831 rates, resulting in temperatures peaking earlier than in the interior BC areas. Accordingly, in this  
832 sub-region, the diabatic term is negative—albeit showing a very strong increase towards near-  
833 zero values when masking for LHF/SM correlation.

834 We finally note that because this budget analysis was undertaken at the 850hPa level, it  
835 may potentially underestimate land-surface processes, but also that the residual diabatic estimate  
836 may also include processes besides land-atmosphere interactions, e.g. related to radiative  
837 heating. However, subsetting for areas typically experiencing land-atmosphere coupling and for

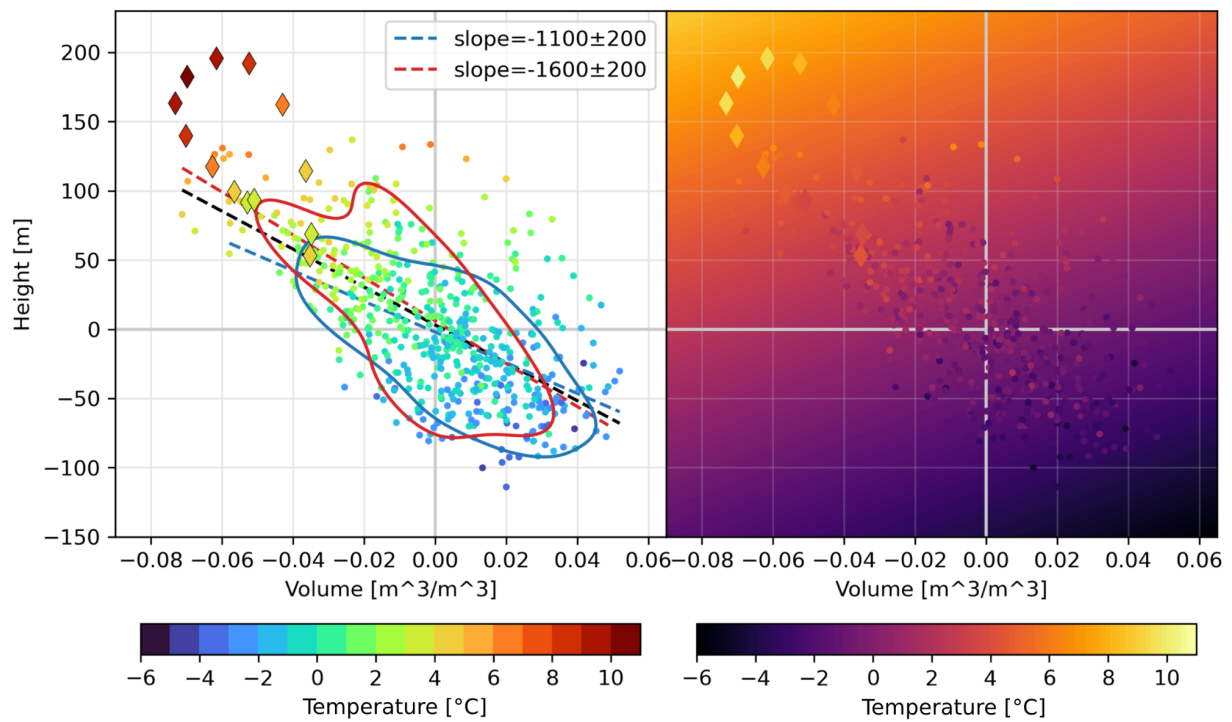
838 where temperature anomalies were highest helps corroborate that the residual term is especially  
839 active both in the regions experiencing the most extreme heat, and where feedbacks may have  
840 been strongest. Both subsets help narrow down that the residual term is likely related at least in  
841 part to land–atmosphere interactions.



842 **Fig. S1: PNW anomalies and actual values compared with historical distributions. Top:** As  
 843 in Figure 1d, but anomalies are not standardized. **Bottom three:** PNW-mean actual variable  
 844 values during June 2021 compared with their historical distributions (over 1981–2010).

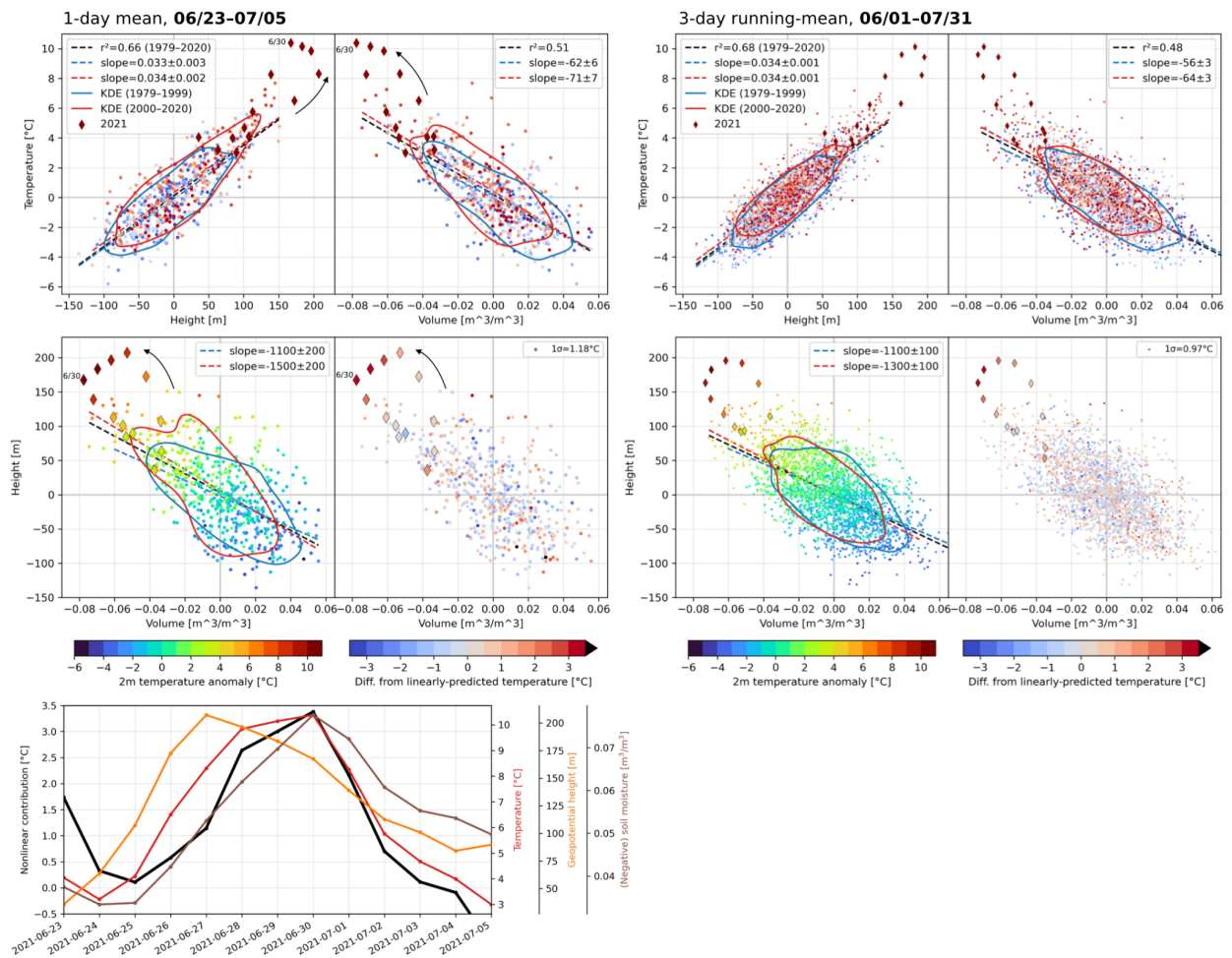


845 **Fig. S2: Total wind, zonal wind, and temperature anomalies in summer 2021. Top:**  
 846 anomalous total wind over 06/25–07/03, with direction in vectors and magnitude in vectors and  
 847 color, compared with climatological total wind speed in gray contours. **Middle:** June-mean  
 848 anomalous zonal wind in color compared with climatological zonal wind in gray contours.  
 849 **Bottom:** 06/15–07/15-mean 2m temperature and zonal wind anomalies and their 10-degree  
 850 smoothings.

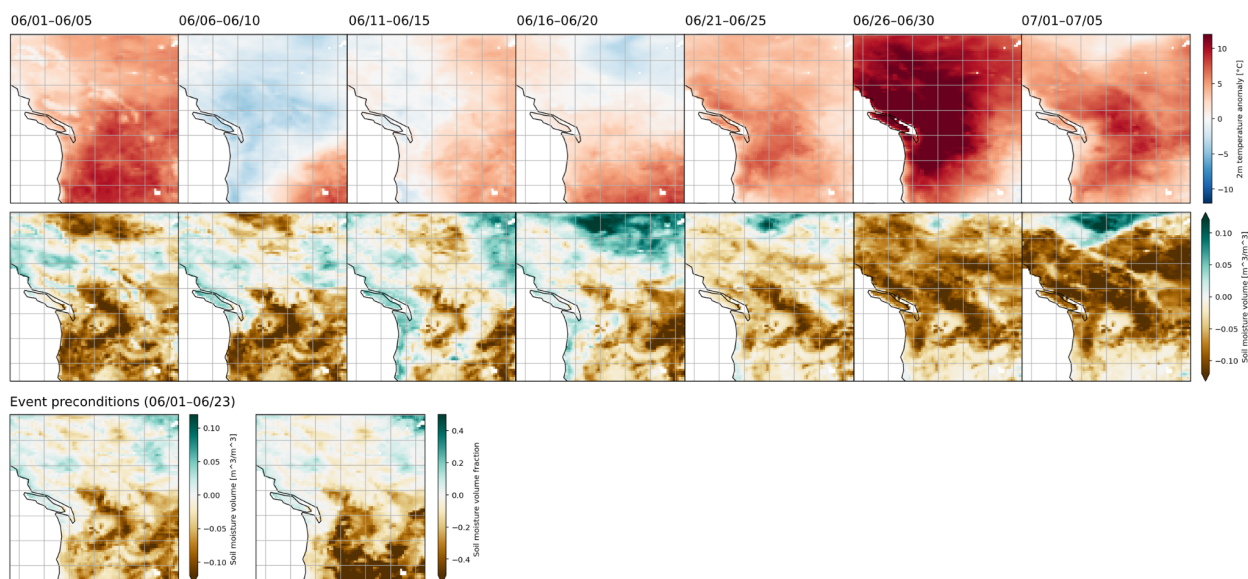


851 **Fig. S3: Comparison of observed temperature versus multiple linear regression prediction.**  
852 **Left panel:** copied from Figure 3 for ease of interpretation. **Right panel:** in the background  
853 gradient, the temperature modeled by a multiple linear regression based on both soil moisture  
854 and geopotential height anomalies, with the regressions calculated from the 3-day mean data  
855 over 06/23–07/05 from 1979–2020. The point data show observed temperatures (i.e., the same  
856 values as shown in the left panel, but according to a different colormap), with dots for 1979–  
857 2020 and diamonds for 2021. The difference between the observed temperature (scattered point  
858 data) and the predicted temperature (the background gradient value underlying each scattered  
859 point) is what is shown in Figure 2d.

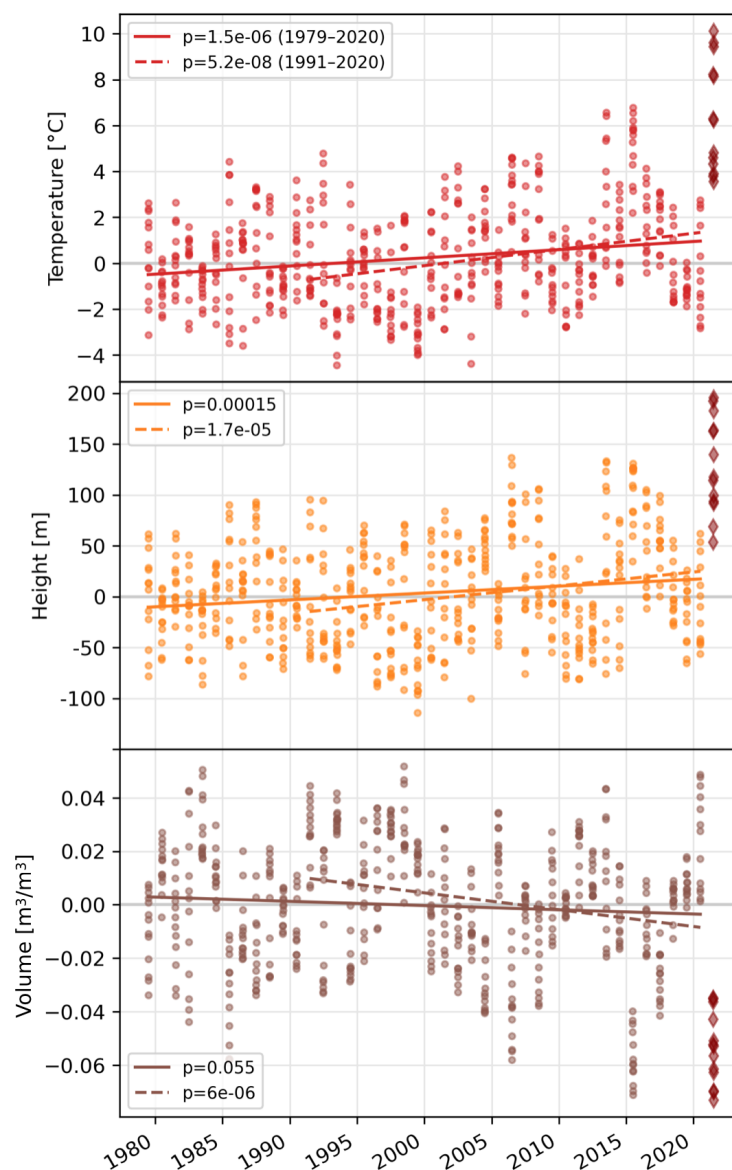




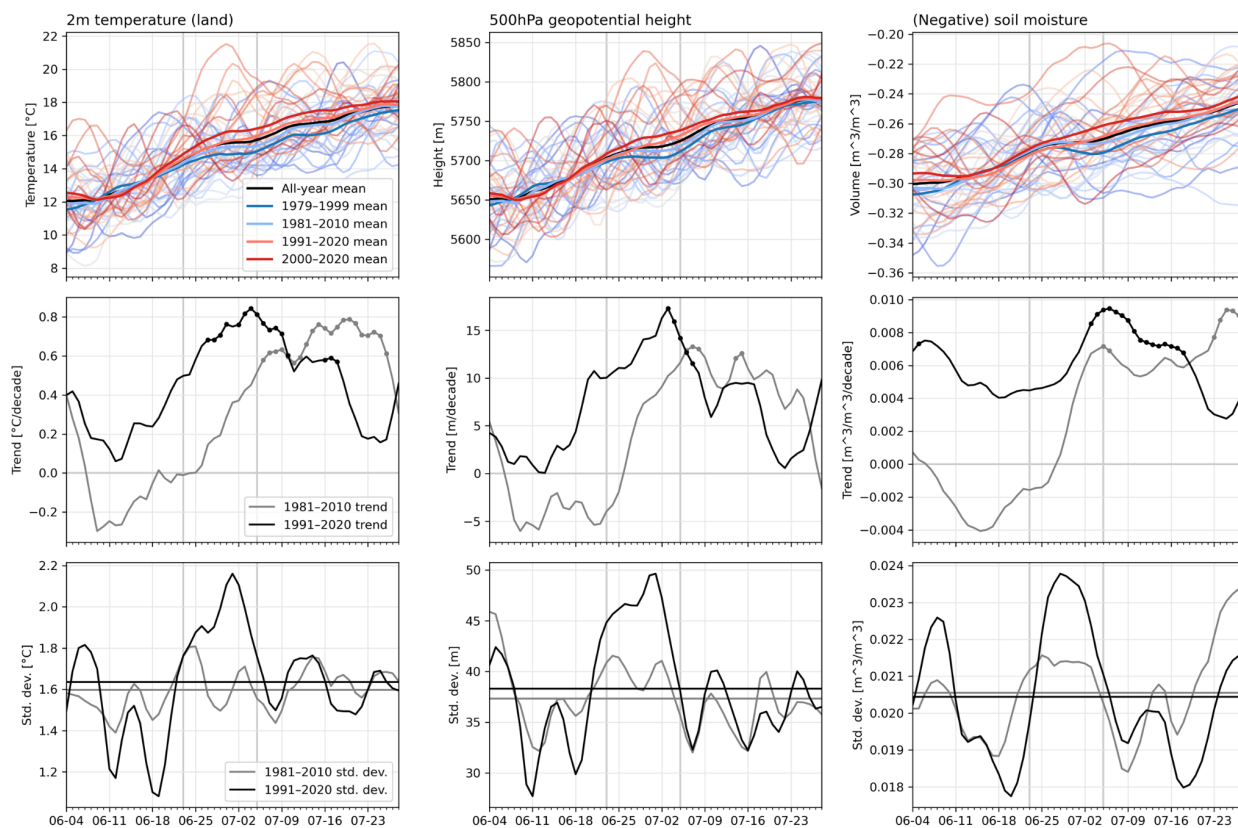
860 **Fig. S4: Top:** As in Figure 2a–d but for daily mean data over 06/23–07/05 (left) and  
 861 3-day running mean data over 06/01–07/31 (right). **Bottom:** daily mean time series of the nonlinear  
 862 contribution term, temperature, geopotential height, and soil moisture anomalies throughout the  
 863 heatwave.



864 **Fig. S5: June evolution of temperature and soil moisture anomalies and soil preconditions**  
 865 **for the late-June heatwave. Top row:** 5-day means of (land) temperature anomalies over the  
 866 PNW from 06/01 to 07/05. **Second row:** as in top row but for soil moisture anomalies. **Bottom**  
 867 **row:** 06/01–06/23 mean soil moisture anomalies over the PNW (left) and the same data  
 868 expressed as fraction of climatology (right), emphasizing large fractional anomalies where soil  
 869 moisture is climatologically low and therefore non-fractional anomalies are limited in magnitude  
 870 compared to wetter areas. (I.e., soil moisture anomalies in Figure 1c show comparatively small  
 871 dry anomalies in the southwest US despite its deep long-term drought, versus the PNW.)

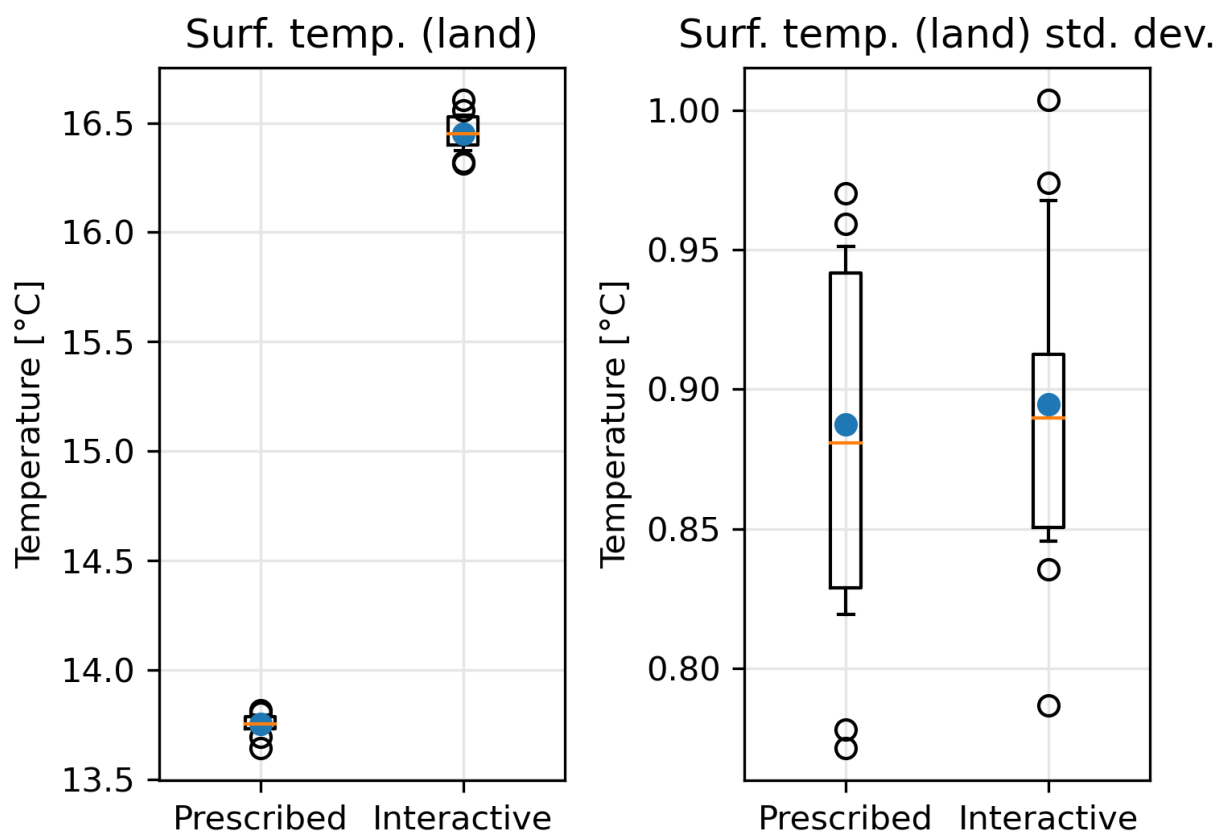


872 **Fig. S6:** The same data as in Fig. 2 plotted against year, shown individually for temperature  
873 (**top**), geopotential height (**middle**), and soil moisture (**bottom**), and linear trends over 1979–  
874 2020 and 1991–2020 (with p-values in legends).

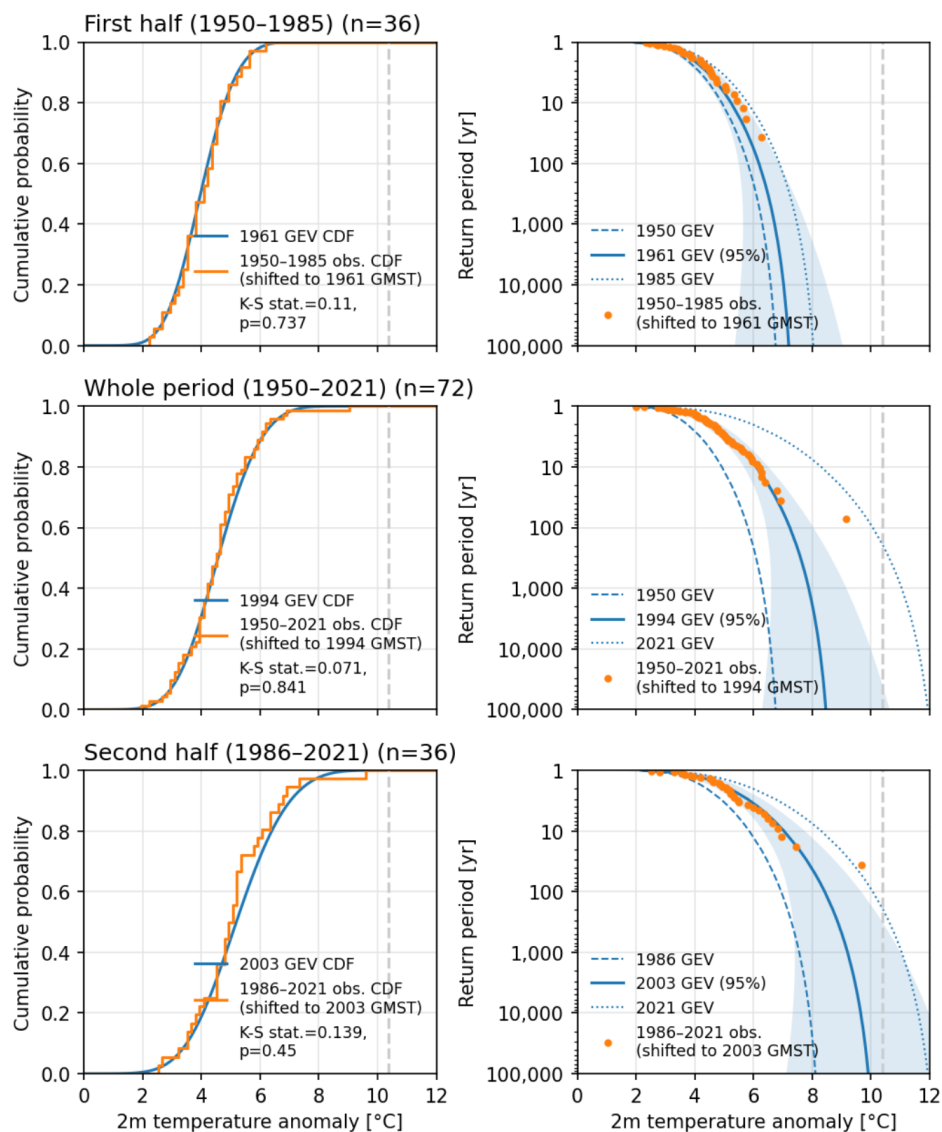


875 **Fig. S7: Historical changes in temperature, geopotential height, and soil moisture and their**  
 876 **interannual variability.** PNW-mean raw (i.e., non-anomalous) temperature, geopotential height,  
 877 and soil moisture data from ERA5 over the entire period of analysis except 2021 (1979–2020,  
 878 throughout June and July). All data are 7-day running means. Gray vertical bars mark 06/23 and  
 879 07/05. **Top row:** color-coded data for each year (blue in 1979 to red in 2020), with means  
 880 throughout the various analysis periods overlaid according to the legend. Second row: linear  
 881 trends in data over 1981–2010 and 1991–2020, marked with dots where significant at 90% level.  
 882 **Bottom row:** interannual standard deviations across 1981–2010 and 1991–2020, with horizontal  
 883 lines demarcating the June–July mean for each period. The bottom row shows that in the PNW,  
 884 standard deviation is increasing for temperature and geopotential height over June and July as a  
 885 whole, and especially for late-June–early-July (when soil moisture standard deviation is also  
 886 increasing sharply)—which is likely associated with warming trends shifting earlier in the year  
 887 in accordance with an advancing summer onset (as illustrated in the left panel of the middle  
 888 row).

### June-mean PNW-mean:

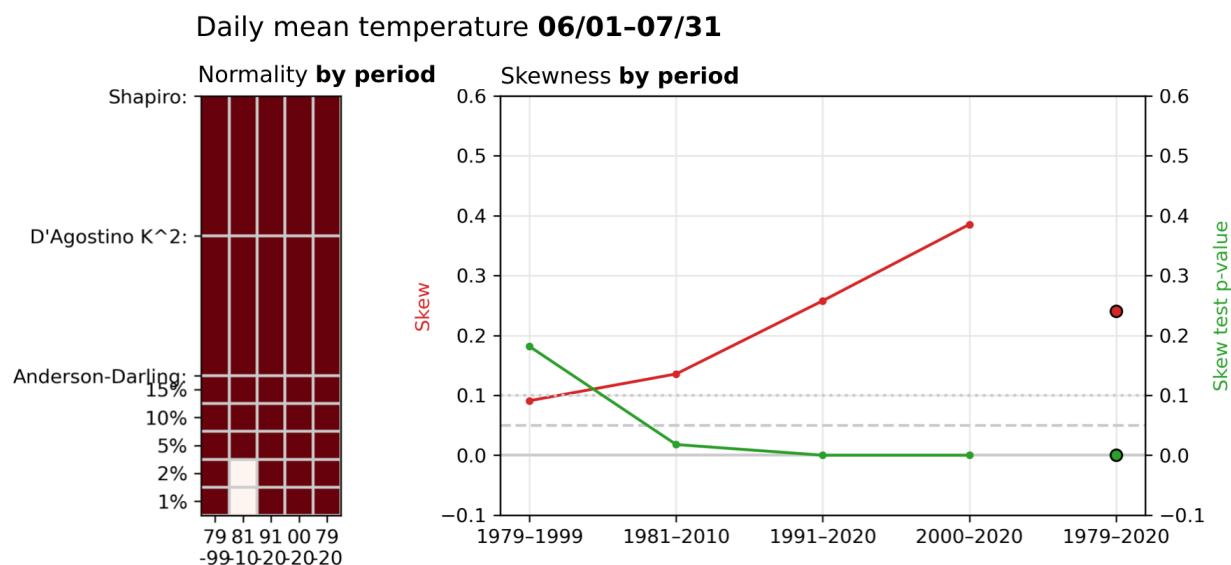


889 **Fig. S8: Shift and variability changes of June-mean PNW-mean temperature in the model**  
890 **experiment.** Boxplots show the model member spread, with the two most distant members  
891 towards either end of the 14-member distribution shown as individual dots. Blue dots show the  
892 ensemble total (all member-months) and orange lines show the ensemble mean. The left plot is  
893 the mean surface temperature, and the right plot is the surface temperature standard deviation.  
894 All standard deviations are calculated internally for each member, i.e., across each member's  
895 entire 1870–2010 run.



896 **Fig. S9: Validation of GEV fits including the 2021 observation.** Left column: For each period, 897 empirical CDFs of observations in that period (orange) are compared with the GEV fit CDF 898 (blue) evaluated at the mean GMST of that period. Results of a Kolmogorov-Smirnov test (D 899 statistic and p-value), testing whether the samples can be determined as drawn from different 900 distributions, are indicated in the legends. No p-values are low enough to reject the GEV fits 901 even with the inclusion of 2021. Right column: For each period, empirical return periods (orange 902 dots) are compared with GEV-derived return periods (blue curves) evaluated at the mean GMST 903 of the period. Empirical return periods are estimated as  $1/(1-i/(n+1))$ , with  $n$  the number of 904 observations in each period and  $i$  their ranking in ascending temperature order. In both columns, 905 the observations' raw temperatures are "shifted", based on the location parameter's dependence

906 on GMST, to each period's mean GMST (for example, the highest temperature observation in  
907 the lower right plot, representing the 2021 heatwave, is shifted down from its raw temperature  
908 [the dashed gray line], to the median GMST of 1986–2021, seen in 2003; compare with Fig. 4b  
909 to see that mean and median are indistinguishable). Shifting observations by GMST in this way  
910 still does not account for any variability changes (i.e., only considers location parameter  
911 nonstationarity, not scale parameter nonstationarity), so K-S tests may even overestimate the true  
912 difference between GEV fits and observations.



913 **Fig. S10: Skew tests for temperature anomaly distributions over historical periods. Top**  
 914 **row:** for daily mean temperature anomalies over 06/23–07/05, the plots show results from three  
 915 normality tests determining whether the dataset (individual days over the 1981–2010 period (left)  
 916 and 1991–2020 period (right)) can be statistically distinguished from normal (red) or not (white).  
 917 Shapiro and D’Agostino tests report a single output, and the Anderson-Darling test reports at 5  
 918 different confidence levels. These results only register interannual variability (one day per year).  
 919 **Bottom row:** The left plot compares the daily temperature anomalies over all of June and July  
 920 subset for 5 different periods (1979–1999, 1981–2010, 1991–2020, 2000–2020, and 1979–2020,  
 921 from left to right). The right plot shows the skewness (red) calculated for temperature data for  
 922 each of the 5 period subsets, along with the *p*-value of the skew test (.1 and .05 significance  
 923 levels indicated). These results register both interannual and intra-annual variability (61 days per  
 924 year over 21- or 30-year periods).



ERA5 data

*Does allowing nonstationarity in the location and/or scale parameters improve the GEV model fit? Finding the test statistic  $D > 0$  indicates improvement, with significance tested according to the critical values in the bottom table.*

	Location	Scale
Fit with 2021	D=18.749 ( <b>p&lt;0.001</b> )	D=6.593 ( <b>p&lt;0.025</b> )
Fit without 2021	D=20.837 ( <b>p&lt;0.001</b> )	D=1.231 (p=0.267)

Model data

*Does allowing nonstationarity in the location parameter improve the GEV model fit?*

	Covariate: PNWMST	Covariate: GMST
Prescribed SM	D=3.573 ( <b>p&lt;0.1</b> )	D=0.461 (p>0.1)
Interactive SM	D=13.836 ( <b>p&lt;0.001</b> )	D=2.400 (p>0.1)

Critical values and significance definitions (from 1-d.o.f. Chi-square distribution):

Critical values of D	D=2.706	D=3.841	D=5.024	D=6.635	D=10.828
Significance if critical value exceeded	p<0.1	p<0.05	p<0.025	p<0.01	p<0.001

925 **Table S1: Likelihood Ratio Test.** The Likelihood Ratio Test (from Theorem 2.7 of Coles et al.  
 926 (2001) tests whether adding nonstationarity in parameters improves the GEV model fit. Tables  
 927 show test statistics (D) and significance levels for adding nonstationarity in the location and scale  
 928 parameters for ERA5 data and nonstationarity in the location parameter for model data, with  
 929 different covariates.